NOVA SCHOOL OF
SCIENCE & TECHNOLOGY

DEPARTMENT OF MECHANICAL
AND INDUSTRIAL ENGINEERING

JOSÉ DAVID FERNANDES CAÇADOR
Graduate in Sciences of Mechanical Engineering

SENSORIAL PROPERTIES ASSESSMENT IN METALLIC PARTS WITH PIEZOELECTRIC PARTICLES

INTEGRATED MASTER IN MECHANICAL ENGINEERING

NOVA University Lisbon
November, 2023

NOVA SCHOOL OF
SCIENCE & TECHNOLOGY

DEPARTMENT OF MECHANICAL
AND INDUSTRIAL ENGINEERING

SENSORIAL PROPERTIES ASSESSMENT IN METALLIC PARTS WITH PIEZOELECTRIC PARTICLES

JOSÉ DAVID FERNANDES CAÇADOR

Graduate in Sciences of Mechanical Engineering

Adviser: Doctor Catarina Isabel Silva Vidal
Assistant Professor, NOVA University Lisbon

Examination Committee

Chair: Doctor Miguel Araújo Machado
Assistant Professor, NOVA University Lisbon

Rapporteur: Doctor Luís Filipe Rosado
Assistant Professor, Instituto Superior Técnico

Adviser: Doctor Catarina Isabel Silva Vidal
Assistant Professor, NOVA University Lisbon

INTEGRATED MASTER IN MECHANICAL ENGINEERING

NOVA University Lisbon
November, 2023

Sensorial properties assessment in metallic parts with piezoelectric particles

---

This document was created with the (pdf/Xe/Lua)LaTeX processor and the NOVAthesis template (v6.10.17) [1].

To my beloved parents, Ricardo and Sandra, for their endless love,
unconditional support, and encouragement.

ACKNOWLEDGEMENTS

I want to express my profound gratitude to my advisor, Professor Dr. Catarina Vidal, for her exceptional guidance, knowledge, organization, concern, availability, and professionalism demonstrated throughout this journey.

To Professor Dr. Telmo Santos, I thank him for his passionate way of teaching and motivating students to be different, ambitious, and with critical thinking.

I thank Master Pedro Ferreira for all the unconditional support, knowledge, patience, and professionalism demonstrated from day one, which were indispensable for completing this work.

To Masters Pedro Fonseca, Pedro Rendas, and Werley Farias, I am grateful for the shared knowledge and how they welcomed and motivated me throughout this journey, making it unique and unforgettable.

To the technicians Mr. António Campos, Mr. Paulo Magalhães, and Master Wagner Sabor, I express my heartfelt thanks for their wisdom, professionalism, and assistance during the experimental phase, which was essential for completing this work.

To my great friends and future Masters, Bernardo Raposo, Daniel Simões, João Filipe, Marcos Esteves, Miguel Matos, and Tomás Narciso I thank you for your help, companionship, and all the moments of fun we shared over the past few years.

To the other professors of Departamento de Engenharia Mecânica e Industrial - DEMI, I would like to express my gratitude for each, in their way, helping me grow and successfully reach this final stage of the course.

I cannot forget Escola Portuguesa de Luanda - EPL, especially teachers Elena Volodina, Grace Ferrão, Arminda Paula, Alexandra Duarte, and Isabel Milheiro, for their excellent teaching, care, and motivation, which made me a better person, more ambitious, and with critical thinking.

Last but not least, I would like to thank my entire family, my parents and my siblings, for their constant presence in my daily life, in my problems, in my decisions, for their understanding, and for the love they have always given to see me happy and succeed.

> *“If you want to change the world, start off by making your bed.”*
>
> *— William H. McRaven*
>
> *(US Navy Admiral)*

ABSTRACT

Predictive maintenance through a condition-based continuous monitoring perspective is a predominant matter in Structural Health Monitoring (SHM). This can be achieved by using embedded sensors (ESs) in structures' metal matrices or through surface sensors (SSs). These last are exposed to external environmental conditions that can be quite severe, damaging sensors and compromising their functionality.

For this reason, there has been an increasing interest in researching ESs and their inherent manufacturing processes by the scientific community. These sensors use smart materials to convert external *stimuli* into electrical output signals.

In the last few years, much effort has been dedicated to assess the possibility of incorporating these materials in metal matrix components. However, conventional manufacturing processes are associated with high processing temperatures due to the fusion of base material. For this reason, solid-state processing techniques have been studied to allow the production of smart materials.

The Research and Development Unit for Mechanical and Industrial Engineering (UNIDEMI) of NOVA School of Science and Technology used Friction Stir Processing (FSP) for the first time to incorporate piezoelectric particles in a work-hardened aluminium alloy AA5083-H111, thus creating a self-sensing material. The purpose of this dissertation was to assess the sensorial properties granted to different heat-treated aluminium alloys, namely AA2017-T451 and AA7075-T651, through the incorporation of Lead Zirconate Titanate (PZT) and Barium Titanium Oxide (BTO) piezoelectric particles, and perform its characterization and comparison between the sensorial properties obtained to AA5083-H111.

Experimental results of this endeavour demonstrated that processing with different heat-treated aluminium alloys did not compromise the sensorial behaviour of the SSMs. However, the sensorial characterisation of the produced SSMs revealed that the obtained sensitivities are lower than those obtained for the AA5083-H111.

Keywords: Smart Materials, Friction Stir Processing (FSP), Sensors, Structural Health Monitoring (SHM), Piezoelectric Particles.

RESUMO

A manutenção preditiva com base na monitorização contínua da condição de estruturas é um tema recorrente em *Structural Health Monitoring* (SHM). Este tipo de manutenção é assegurado através da utilização de sensores embutidos na matriz metálica das estruturas, apesar de também poderem ser colocados superficialmente nas mesmas. Neste último caso, os sensores encontram-se expostos às condições externas que podem ser bastante severas ao ponto de os danificarem, comprometendo a sua funcionalidade.

Por este motivo, o recurso a sensores embutidos, assim como os processos de fabrico inerentes, têm vindo a ser vastamente estudados pela comunidade científica. O funcionamento destes sensores baseia-se na utilização de *smart materials* que são capazes de converter estímulos externos aplicados à estrutura em sinais elétricos.

Nos últimos anos, vários estudos têm sido realizados para avaliar a possibilidade de incorporação destes materiais em componentes de matriz metálica. Contudo, os processos de fabrico convencionais estão associados a elevadas temperaturas de processamento decorrentes da fusão do material base. Neste sentido, diversas técnicas de processamento no estado sólido têm vindo a ser estudadas para permitir a produção dos *smart materials*.

A Unidade de Investigação e Desenvolvimento em Engenharia Mecânica e Industrial (UNIDEMI), da NOVA School of Science and Technology | FCT NOVA, utilizou pela primeira vez o Processamento por Fricção Linear (FSP) para incorporar partículas piezoelétricas numa liga de alumínio endurecida por trabalho mecânico AA5083-H111, criando assim um material autossensível. Esta dissertação pretendeu avaliar as propriedades sensoriais obtidas em ligas de alumínio tratadas termicamente, nomeadamente a AA2017-T451 e a AA7075-T651, através da incorporação de partículas piezoelétricas de Titanato Zirconato de Chumbo (PZT) e Titanato de Bário (BTO), e proceder à sua respetiva caracterização e comparação com as propriedades sensoriais da liga AA5083-H111.

Os resultados experimentais demonstraram que o processamento com ligas de alumínio tratadas termicamente não comprometeu o comportamento sensorial dos SSMs. Contudo, a sua caracterização sensorial revelou que as sensibilidades obtidas são inferiores às obtidas para a liga AA5083-H111.

Palavras-chave: Materiais Inteligentes, Sensores, Processamento por Fricção Linear, Monitorização da Integridade Estrutural, Partículas Piezoelétricas.

CONTENTS

LIST OF FIGURES

List of Tables

Acronyms

AS	Advancing Side *(pp. 26, 34, 38, 58)*
BTO	Barium Titanate Oxide *(pp. vi, vii, x, 2, 21–24, 33, 38, 40–42, 45, 50, 51, 54, 55, 58–60)*
EDX	Energy Dispersive X-Ray *(pp. x, xi, 23, 29, 38, 40–45)*
EFPI	Extrinsic Fabry-Perot Interferometric *(pp. 10, 11)*
ESs	Embedded Sensors *(pp. vi, 1, 2, 10, 16, 18)*
FBG	Fibre Bragg Grating *(pp. 10–13, 17)*
FGMs	Functionally Graded Materials *(p. 18)*
FOSs	Fibre Optic Sensors *(pp. xiii, 10, 11, 16, 17, 19, 20)*
FSP	Friction Stir Processing *(pp. vi, vii, x, xi, 2, 17, 18, 21, 22, 25, 26, 34, 36–38, 41, 44, 50, 54, 59, 60)*
FSW	Friction Stir Welding *(p. 18)*
HAZ	Heat-Affected Zone *(pp. 38, 39, 54)*
LPG	Long-Period Grating-Based *(pp. 10, 11)*
MEMSs	Microelectromechanical Systems *(pp. 4, 18)*
MMCs	Metal Matrix Composites *(p. 17)*
OTDR	Optical Time Domain Reflectometer *(pp. 11, 12)*
PSs	Piezoelectric Sensors *(pp. xiii, 10, 16, 17, 20, 21)*
PVDF	Polyvinylidene Fluoride *(pp. 14, 20, 21)*
PZT	Lead Zirconate Titanate *(pp. vi, vii, x, 2, 14, 20, 22–24, 33, 40, 41, 43, 45, 50, 51, 54, 55, 58–60)*
RS	Retreating Side *(pp. 26, 34, 38, 58)*
SEM	Scanning Electron Microscopy *(pp. x, xi, 23, 24, 29, 41–45, 48, 59)*

SHM	Structural Health Monitoring *(pp. vi, vii, 1, 2, 11)*
SMA	Shape Memory Alloy *(pp. x, 2, 6, 7, 16)*
SME	Shape Memory Effect *(pp. 6, 7, 15)*
SSM	Self-Sensing Material *(pp. vi, vii, xi–xiii, 2–4, 15, 18, 22, 23, 25, 28–31, 33, 34, 37–40, 45–51, 54–61)*
SSs	Surface Sensors *(pp. vi, 1)*
ST	Sensing Technology *(p. 1)*
TMAZ	Thermo-Mechanically Affected Zone *(pp. 38, 39, 59)*
UAM	Ultrasonic Addictive Manufacturing *(pp. x, 17–19, 21)*

Symbols

A	Amplitude applied during sensorial tests *(pp. xii, 31, 54, 56)*
T_c	Curie temperature *(pp. 24, 25)*
d	Density *(p. 25)*
K_{33}	Dielectric constant *(p. 25)*
k_{33}, k_{31}	Electromechanical coupling coefficient *(p. 25)*
f	Frequency applied during sensorial tests *(pp. xii, 31, 54–56)*
E	Modulus of elasticity *(pp. 23, 50)*
d_{33}, d_{31}	Piezoelectric constant *(p. 25)*
ω	Rotation speed *(pp. 32, 33)*
$\varepsilon_{\mathbf{f}}$	Strain at fracture *(p. 50)*
t	Thickness of specimens used for tensile and sensorial tests *(p. 29)*
v	Travel speed *(pp. 32–34)*
$\sigma_{\mathbf{UTS}}$	Ultimate tensile strength *(pp. 23, 50, 59)*
$\sigma_{\mathbf{0.2}}$	Yield strength *(pp. 23, 50, 59)*

1

Introduction

1.1 Contextualisation

Structural Health Monitoring (SHM) consists of monitoring structures or components in real-time and throughout their life cycle, namely by using Surface Sensors (SSs) or Embedded Sensors (ESs), without compromising their structural integrity [2, 3].

This topic has been arousing the scientific community's interest, given the possibility to revolutionise how maintenance of structures has been implemented, starting to be a condition-based predictive approach based on a continuous-monitoring perspective rather than a preventive or corrective one. Therefore, extending the structure or component life cycle while reducing costs regarding its replacement and qualified labour working [3].

The main types of maintenance are depicted in Figure 1.1, presented bellow.

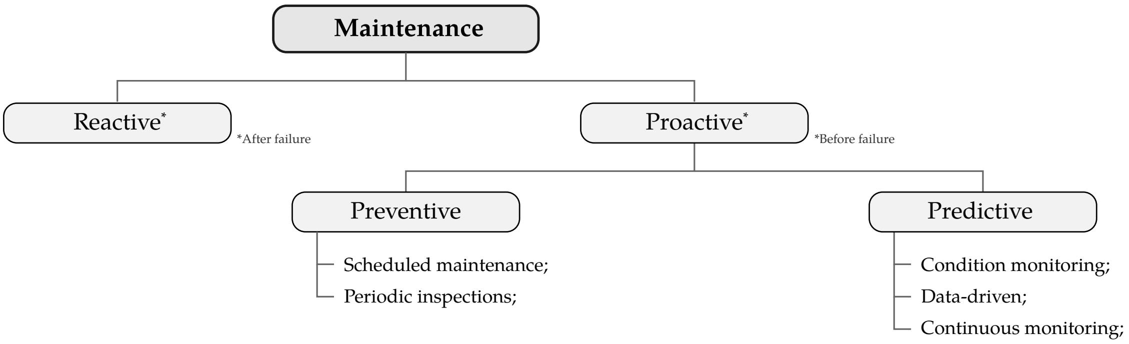

Figure 1.1: Schematic of types of maintenance

Furthermore, continuous monitoring provides an information record regarding the environmental conditions applied to the structure, while periodic inspections are unable to provide any information on accidents or failures that occur between two successive revisions [2].

Sensing Technology (ST) is responsible for developing these sensors, sensory systems, or smart materials with the capacity to continuously monitor these structures and ensure permanent measures used to evaluate their structural integrity [2].

Smart material systems are often hybrid composite or integrated systems of materials with several advantages and capabilities over the existing conventional functional materials. They are currently being implemented in various industries, including automotive, aerospace, military, mechanical and biomedical engineering, energy, electronics, chemical, nanomedicine, cell recovery, disease therapy, and civil engineering [4].

Piezoelectric [2–22], Shape Memory Alloys (SMAs) [2, 4, 6–10, 23], and Fibre Optics [2, 4, 6–10, 24–43] are some of the most commonly used smart materials for SHM.

1.2 Motivation and objectives

This dissertation presents an extensive literature review regarding smart materials and a state-of-the-art review concerning its applications to manufacturing ESs in metallic parts.

Over the last decade, fibre optics and piezoelectric materials have been successfully incorporated into metallic parts to produce self-sensing materials (SSMs). More recently, Friction Stir Processing (FSP) was reported to be a promissory process technology to grant sensorial properties to an annealed and slightly strain-hardened AA5083-H111 plate through the incorporation of barium titanate and lead zirconate titanate piezoelectric particles [3, 44].

The main objective of this dissertation was to grant sensorial properties to heat-treated AA2017-T451 [45] and AA7075-T651 [46] aluminium plates through the incorporation of Lead Zirconate Titanate (PZT) and Barium Titanium Oxide (BTO) particles using FSP. Furthermore, it is intended to compare its sensitivities with the AA5083-H111 SSM by conducting a set of dynamic solicitations to evaluate its sensorial properties. Additionally, the produced SSMs must be subjected to metallographic and physicochemical characterisation to assess the distribution and concentration of the particles within the aluminium matrix. The mechanical properties are also an object of study to evaluate the impact of incorporating these piezoelectric particles into the metal.

1.3 Dissertation's structure

This report is structured into five chapters, introduction, literature review, experimental methodology, experimental results and conclusions and future works.

The introduction explains the contextualization and motivation of this dissertation while briefly describing the overall panorama of the state-of-the-art. It also presents the objectives of this work and its structure.

The literature review commences by defining smart materials, their classification and the characteristics of the most relevant smart materials. Then, an in-depth research is performed to assess how some of these materials may be integrated into materials to create sensorial devices capable of measuring external *stimuli* such as stress, strain, or temperature. Ultimately, a state-of-the-art revision is conducted regarding the embedment of such materials into metallic parts and the associated technological processes and challenges.

The third chapter presents the adopted experimental methodology for the conducted experimental procedures. It entails a characterisation of the base materials and a characterisation of the piezoelectric particles. The various methods employed for characterising the SSM are described, including the utilized equipment, experimental setups, and measurements carried out during its production.

The following chapter addresses aspects such as selecting processing parameters for the SSM production. Additionally, it presents the temperature data collected during its processing and the experimental results obtained from the characterisation techniques employed.

Finally, the fifth chapter presents the conclusions of the work undertaken and suggestions for future works regarding this subject.

2

Literature review

2.1 Smart materials

Science and technology have advanced remarkably in synthesizing new materials over the last two decades. These can be primarily classified into four categories: polymers, ceramics, metals, and smart materials [6].

Smart materials are usually related to composite materials embedded with fibre optics, actuators, sensors, microelectromechanical systems (MEMSs), vibration control, sound control, shape control, product health or lifetime monitoring, cure monitoring, and intelligent processing [6].

Using these materials instead of conventional methods to sense and respond can simplify devices, reducing weight and the chance of failure while improving design flexibility, functionality, reproducibility, and reliability [6].

These SSMs, also designated as intelligent materials, might be one of the most promising developments for a more sustainable and less energy-consuming world [6].

2.1.1 Definition

Different authors have proposed several definitions to describe and characterise smart materials. Lefebvre Esther et al. [7] propose a more generalist definition, describing smart materials as materials that change properties according to *stimuli*, adapting to their environment, whereas John McCabe et al. [47] present a more complete definition regarding the ability to return to the original state after the stimulus has been removed. Therefore, smart materials are also characterised as responsive [4] and reversible [9] materials.

These materials have an inherent capacity to manifest a response upon the application of different *stimuli*, as suggested in Figure 2.1.

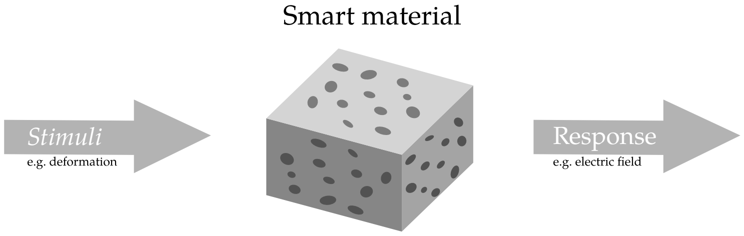

Figure 2.1: Basic functioning of smart materials [3, 7]

2.1.2 Classification

Efforts have been made to sort these materials and separate them by *stimuli* and response, representing their main functionality in terms of materials selection criteria (Ashby et al., 2002), as illustrated in Figure 2.2 [7].

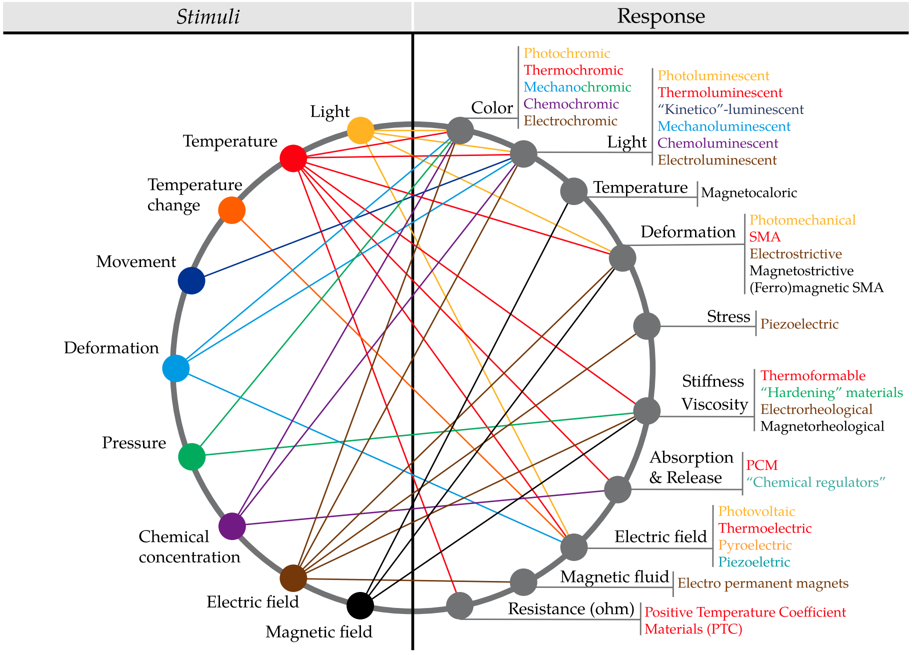

Figure 2.2: Classification of smart materials based on *stimuli* and response [7]

Furthermore, smart materials can be classified as active or passive regarding their ability to transduce energy. While active smart materials have an intrinsic ability to transduce energy, passive do not. For instance, piezoelectric materials are active smart materials, while fibre optic is passive. Besides, passive materials can be applied as sensors but not as actuators [4].

2.1.3 Active smart materials

2.1.3.1 Piezoelectric materials

The origin of piezoelectricity comes from the Greek word *piezein*, which means to press, and *elektron*, referring to amber, an ancient source of electric charge [4].

Each cell or molecule in these materials is a dipole with a positive and negative charge on either end. The alignment of these internal electric dipoles may result in a surface charge, but this charge is neutralized by free charges present in the surrounding atmosphere. When a force is applied to the piezoelectric material, causing deformation to take place, the neutralized state of the surface is altered by changing the orientation of the dipoles, producing an electric potential as response [9]. This is known as the direct piezoelectric effect. The converse piezoelectric effect occurs when an applied electric potential causes polarized molecules to align themselves with the electric field, which, in turn, causes a deformation to develop [8].

The piezoelectric behaviour is depicted in Figure 2.3.

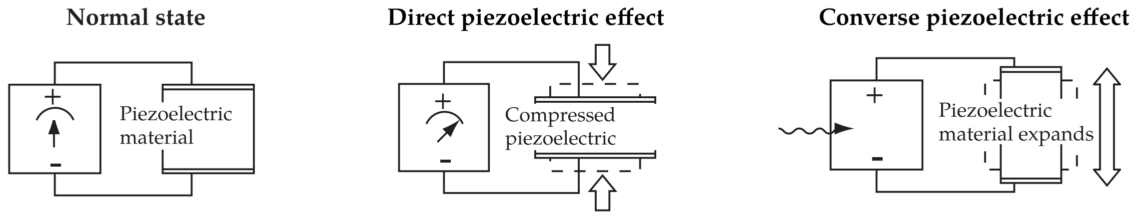

When deformed by a force, a voltage output is generated

When a voltage is applied, a deformation results

Figure 2.3: Piezoelectric behaviour [9]

Since the discovery of the piezoelectric phenomena, dating back to 1880 by the Curie brothers, several synthetic and natural materials have been discovered to have piezoelectric properties. These can be classified into four classes: natural crystals, liquid crystals, noncrystalline materials textures, and synthetic piezoelectric materials, as presented in Table 2.1 [4].

Table 2.1: Synthetic and natural piezoelectric materials [4]

Natural crystals	**Liquid crystals**	**Noncrystalline materials textures**	**Synthetic piezoelectric materials**
Quartz, rochelle salt, ammonium phosphate	Ferroelectric liquid crystals (FLCs)	Glass rubber, paraffin, bone, wood	1. Piezoceramics: lead zirconate titanate, lead niobate, lead lanthanum zirconate titanate 2. Crystallines: ammonium dihydrogen phosphate 3. Piezoelectric polymer: polyvinylidene fluorite

2.1.3.2 Shape memory alloys

SMAs derive their unique transducer capabilities from the fact that they can recover from up to 10% strains through temperature and stress-induced transformations between high-temperature austenite and low-temperature martensite phases [10].

The phenomenon that governs these materials is known as the shape memory effect (SME) and relies on these two temperature-dependent stable phases. The high-temperature austenite phase, also called parent or memory phase, has a body-centred cubic crystal structure, while the low-temperature martensite phase is characterised by a lower symmetry, with a tetragonal, orthorhombic, or monoclinic crystal structure [23].

The martensite assembly can exist in two forms: twinned and de-twinned. The twinned martensite is formed by a combination of self-accommodated martensitic variants, whereas a specific variant is predominant in the de-twinned martensite [23].

Due to the differing crystallographic structures, both martensite and austenite phases have very different mechanical, thermal, electrical, acoustic, and optical properties. Their thermodynamic stability allows SMAs to remember various shapes constructed in the austenite phase [10].

An SMA exhibits the SME when deformed at a low temperature by retaining an apparent plastic deformation upon unloading. Subsequently, if it is heated above A_f, the temperature at which transformation from the martensite phase into austenite finishes, it recovers its original shape. This behaviour, presented in Figure 2.4, can be interpreted in light of the phase transitions and reorientation of martensite variants [23].

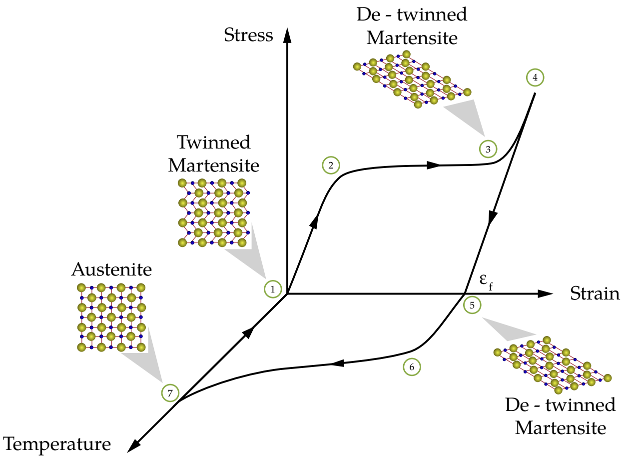

Figure 2.4: Shape memory effect [23]

This is also known as one-way SME because only the high-temperature shape is memorized by the material. Indeed, no change in shape occurs upon cooling under no applied load, even though the crystallographic transition from austenite to martensite is present (Fig. 2.4, points 7-1) [23].

SMAs may also present a two-way SME when subjected to specific thermomechanical training. In this case, the material can reversely restore the shapes of both austenitic and martensitic phases. This property moves between the two mechanical configurations simply by changing the temperature, with no need for an applied load [23]. The two-way SME is schematically represented in Figure 2.5b.

Although the one-way SME is an intrinsic characteristic of SMAs, two-way memory requires inducement by specific treatments such as training, as mentioned previously, which in turn involves the deformation of martensite or different repeated temperature-stress cycles [23].

To date, many alloys have been studied for exhibit SME, namely copper-based alloys such as CuZnAl and CuAlNi, and iron-based alloys such as FePt, FePd, and FeMnSi. Nevertheless, Nitinol, a NiTi alloy, is still the most used alloy with the best general shape memory characteristics, together with three other advantageous properties: excellent corrosion resistance, a stable configuration, and almost perfect biocompatibility [23].

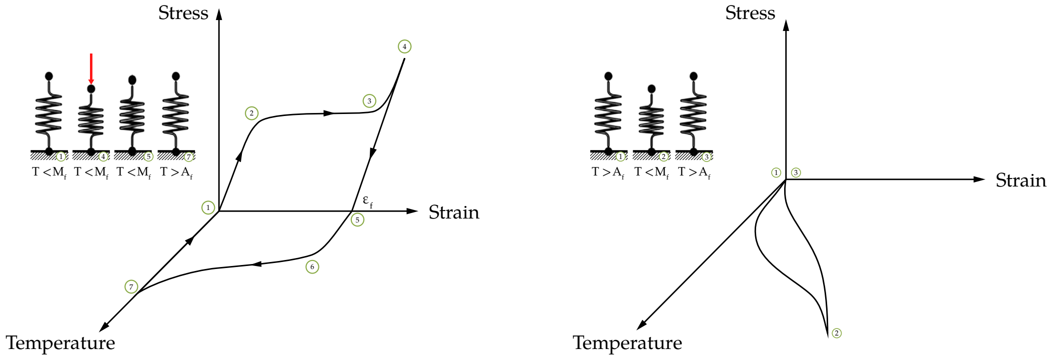

(a) (b)

Figure 2.5: SME: one-way (a); two-way (b)

2.1.3.3 Electrorheological and magnetorheological fluids

Electrorheological (ER) and Magnetorheological (MR) fluids are characterised by reversible changes in the rheology of the fluids when subjected to electric or magnetic fields [10].

As illustrated in Figure 2.6, these fluids are comprised of several particles, typically $1 - 10\ \mu$m in size, suspended in inert fluids such as mineral or silicon oils. In the absence of applied fields, these particles are uniformly distributed and, to a first approximation, the fluids are characterised as Newtonian [10].

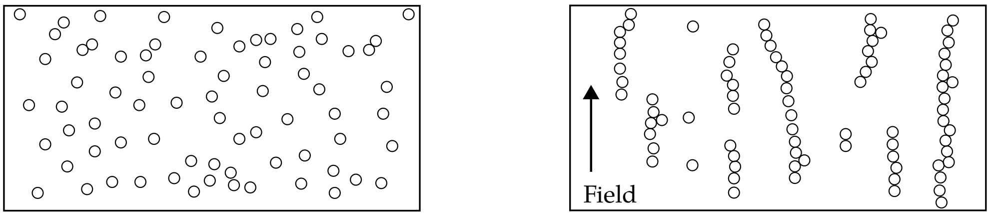

(a) (b)

Figure 2.6: MR and ER fluids: no applied field (a); applied electromagnetic field (b) [10]

Applying an applied electric field, E, or magnetic field, H, causes the particles to align in chains, also called tendrils or fibrils, with the same field direction, which promotes changes in the shear stress of the fluid [10].

2.1.3.4 Magnetostrictive and electrostrictive materials

Magnetostrictive materials exhibit changes in mechanical strain when subjected to a magnetic field. Reversibly, when mechanical stress (or strain) is applied to the material, it changes its magnetization. Hence, these materials can be used as sensors and actuators due to the direct and converse effects [4, 8].

Nickel was the first known magnetostrictive material. However, Terfenol-D is the most popular commercially available magnetostrictive material [4, 8].

The electrostrictive phenomenon is a nonlinear property that exists in all dielectric materials. When an electric field is applied across an electrostrictive material, the positive and negative ions are displaced, and a strain is induced in the material. The resulting strain is proportional to the square of the applied electric field and is independent of the applied electric field's polarity. Because the strain is proportional to the square of the electric field, the strain is always positive. This is analogous to the magnetostrictive behaviour mentioned above [8].

The most commonly used electrostrictive material is Lead Magnesium Niobate (PMN). Due to nonlinear behaviour, these materials generally offer higher electrically induced strain with lower hysteresis than piezoelectric materials. However, constitutive models for electristrictors are less mature than models for piezoelectrics [8].

2.1.4 Passive smart materials

2.1.4.1 Fibre optics

Optical fibres operate by the principle of total internal reflection, which occurs when light encounters an interface with a material with a lower refractive index, $n_2 < n_1$. When the angle of incidence, θ_i, is greater than the critical angle of incidence, θ_c, total internal reflection occurs, and optical fibres act as light guides in the manner depicted in Figure 2.7c. In this regime, the radiation also satisfies the law of reflection, which states that the angle of incidence is equal to the angle of reflection, $\theta_i = \theta_r$ [10].

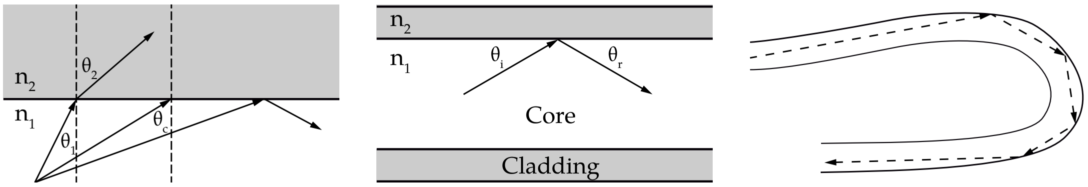

(a) (b) (c)

Figure 2.7: Fibre optic principles: refraction and reflection of light at the interface between materials with refractive indices n_1 and n_2, $n_1 > n_2$ (a); reflection of light, $\theta_i > \theta_c$ (b); travel of light within an optical fibre (c) [10]

2.2 Sensorial devices using smart materials

2.2.1 Sensors, transducers and actuators

A sensor is a device that detects or responds to a physical or chemical stimulus, such as motion, heat, or chemical concentration. It directly interacts with the stimulus field, involving an exchange of energy or a conversion of energy from one form to another [9].

Sensors and transducers are closely related to one another since both involve energy exchange. A transducer is a device that converts energy from one form to another, namely mechanical energy into electrical energy, although it can also transfer it in the same form. Transducers are generally used to transmit, monitor, or control energy. Contrastingly, sensors – which also involve energy exchange – interact directly with and respond to the surrounding stimulus field [9].

An actuator is a device that converts an input energy signal into a mechanical or chemical action. These devices are typically used for controlling purposes to produce a mechanical movement in response to an input electrical potential [9].

The same device may serve as an actuator and sensor since some smart materials present a bi-directional behaviour. Piezoelectric devices can act as actuators when an external stimulus of electric potential produces a mechanical deformation on the material or as a sensor if the opposite is verified [9].

The performance of any sensor can be evaluated in terms of sensitivity, i.e. the produced signal's intensity for a given change in the input signal, bandwidth, i.e. the frequency range over which the sensor remains effective, response time, i.e. the speed at which the sensor can respond to a change in the variable, the temperature range across which the sensor can operate, the length across which the measurement is made, the repeatability and precision of the actuator, weight, and cost [8].

Over the last years, many sensors and sensing techniques have been developed for health monitoring. The most relevant applications are Fibre Optic Sensors (FOSs) and Piezoelectric Sensors (PSs). These sensors can be embedded in materials due to their reduced size. Also, FOSs are most suited for internal measurement by ESs due to their size, weight, high flexibility and long-term durability [8].

2.2.2 Fibre optic sensors

As stated in Section 2.2.1, FOSs are well-suited for *in situ* monitoring of the internal state of materials. These can be embedded to quantitatively monitor internal strain and temperature and have been used since the early 1990s [8].

These sensors are made of long-lasting materials, namely silica and sapphire, capable of resisting corrosion and high tensile loads. While the silica core enables measurements of temperatures on the order of 200 to 800 ºC, the sapphire core goes up to 1500 ºC, both capable of exhibiting resolutions on the order of 0.1 ºC [2].

There are many kinds of FOSs, including intensity-based sensors, interferometric sensors, polarimetric sensors, Extrinsic Fabry-Perot Interferometric (EFPI) sensors, Fibre Bragg Grating (FBG) sensors, Long-Period Grating-Based (LPG) sensors, Raman scattering sensors, and Brillouin scattering sensors, as presented in Table 2.2 [8].

As stated previously, these sensors can measure temperature since their reflective index is sensitive to temperature. However, temperature compensation might be necessary if the sensors are placed in a large temperature variation environment to guarantee the precision of strain measurements [8].

These sensors are also used for damage detection by measuring strain distribution to estimate the location of the damaged area analytically. However, some types of FOSs have the potential for directly detecting damages, which means that changes in signals directly

Table 2.2: Fibre-optic sensors for *in situ* health monitoring [8]

	Monitored Value	**Multiplexing/ Distributing**	**Gauge Length**	**Sensor Cost**	**System Cost**
Intensity-based	Break, microbend, strain, vibration	OTDR	Short/ Long	Cheap	Cheap
Interferometric	Strain, temperature, vibration	Switching	Long	Cheap	Middle
Polarimetric	Strain, temperature, vibration	Switching	Long	Cheap	Middle
EFPI	Strain, temperature, vibration	Switching/Frequency domain	Short	High	Middle-High
FBG, LPG	Strain, temperature, chemical property	Frequency domain (Easy multiplexing)	Short	High	High
Raman scattering	Temperature	OTDR (ROTDR)	Variable	Cheap	High[a]
Brillouin scattering	Strain, temperature	OTDR (BOTDR)	Variable	Cheap	High[b]

[a] Not including OTDR.

[b] Includes OTDR.

indicate damage initiation and development without an analytical identification. These sensors must be placed near the damaged region because the sensing area of the FOSs is limited to its proximity [8].

Using FOSs to achieve a practical SHM system relies on distributing and multiplexing techniques. Three configuration techniques, optical switching (parallel multiplexing), serial multiplexing, and distributing, are depicted in Figure 2.8 [8].

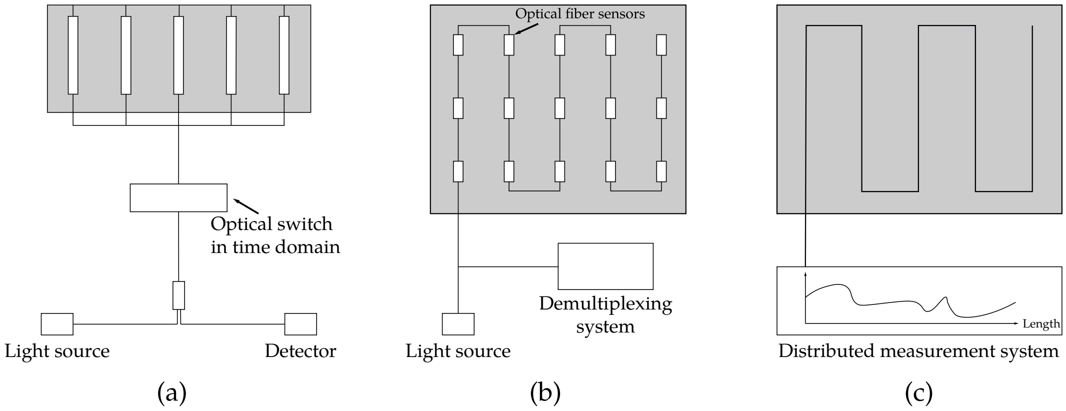

Figure 2.8: Configurations of distributing and multiplexing techniques: optical switching technique (a); serial multiplexing technique (b); distributing technique (c) [8]

The optical switching technique is used when the system involves multiple FOSs. However, this technique is not ideal due to its low switching speed. Interferometric and polarimetric FOSs can be multiplexed by optical switching devices [8].

The serial multiplexing technique is typically used for short-gauge sensors such as intensity-based strain sensors, EFPI sensors, and FBG sensors [8].

2.2.2.1 Intensity-based strain sensors

Intensity-based sensors can be multiplexed by an Optical Time Domain Reflectometer (OTDR). An OTDR is a popular distribution sensing technique along a single fibre. It consists of a short-pulse laser and a high-speed detector capable of scanning the location of the reflection through a single fibre in the time domain. The resolution of OTDR depends on the pulse width, which is from several hundred millimetres to several metres. Raman scattering sensors and Brillouin scattering sensors are generally used with an OTDR. Intensity-based fibre optic sensors have several configurations, as depicted in Figure 2.9 [8].

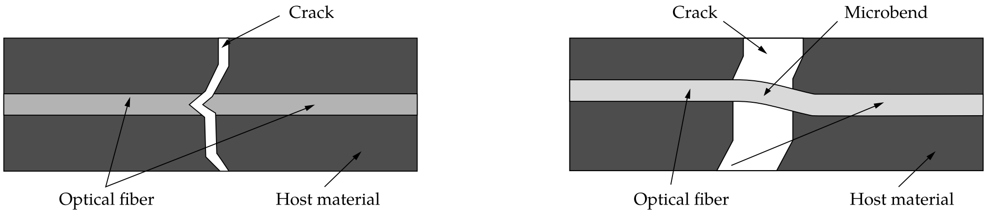

(a) Break sensor (b) Microbend sensor

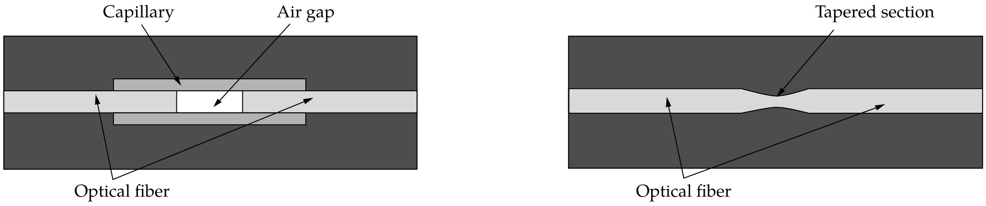

(c) Gapped strain sensor (d) Tapered (or profile) strain sensor

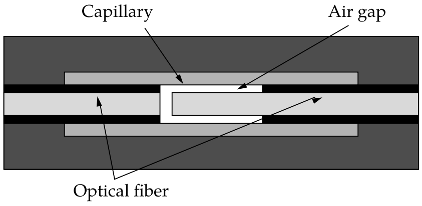

(e) Vibration sensor

Figure 2.9: Intensity-based fibre optic configurations [8]

2.2.2.2 Fibre optic strain gauges

There are two primary types of fibre optic strain gauges, Fabry–Perot and FBG sensors. Both types offer several advantages over traditional resistance strain gauges. Because fibre optic strain gauges use light as the sensing and transmitting element, they are intrinsically safe and pose no fire or explosive hazards. Furthermore, fibre optics are very resistant to corrosive elements because they have no metallic components and are covered by protective hermetically sealed coatings. A final common advantage is that fibre optics are immune to electromagnetic interference. Therefore, they can be placed in regions of high electric or magnetic fields without any performance degradation. Both types of fibre optic strain gauges can also have resolutions equal to or greater than resistance strain gauges [8].

Fabry–Perot fibre optic strain gauges

Fabry–Perot strain gauges are manufactured by placing a small air gap, or resonance cavity, within a fibre followed by a partially-reflective surface, which can be either a micromirror or more optic fibre. A broadband light wave is transmitted down the length of the fibre. At the first junction between the fibre and the air gap (or mirror), some light is reflected back to the source, and some light is transmitted into the gap. At the second air-fibre interface, light is again reflected and transmitted. Now, two separate light sources reflect light back along the length of the fibre. The air gap length dictates the phase difference between the two waves. Reflected light from the Fabry-Perot sensor is transmitted maximally where the optical path length matches the dimension of the Fabry-Perot cavity. Allowing this air gap to expand or contract, based on the local strain, creates a strain sensor. Hence, a phase offset measurement can be correlated to a strain measurement [8].

There are extrinsic Fabry–Perot sensors, intrinsic Fabry–Perot sensors, and in-line fibre etalon (ILFE) sensors. All three are based on the same principle, the differences lie in the choice of the reflective medium. Although intrinsic Fabry–Perot sensors are sensitive to strain and temperature, extrinsic Fabry–Perot sensors, depicted in Figure 2.10, and ILFEs have very low thermal sensitivity. One disadvantage of Fabry–Perot sensors, compared to fibre Bragg grating sensors, is the difficulty in multiplexing many sensors along a single fibre [8].

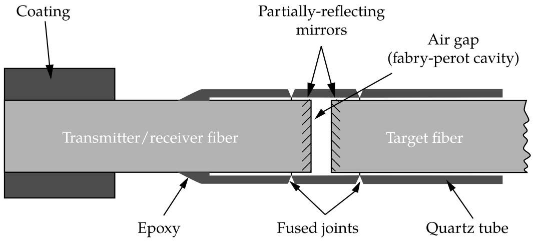

Figure 2.10: Schematic representation of an extrinsic Fabry-Perot interferometer [8]

Fibre Bragg Grating strain gauges

FBG sensors are based on the photorefractive effect. There are several imprinting methods to fabricate these sensors, namely interferometric or phase masks methods, using ultraviolet laser. It consists on exposing bare fibre to a hydrogen environment where it is imprinted using an ultraviolet laser, which leaves a series of equally spaced regions along a small fraction of the fibre. This regions are also called a Bragg grating and have a slightly different index of refraction [8].

The transmitted radiation through the fibre is reflected back towards the source at a specific frequency that corresponds to the grating wavelength. All other frequencies of radiation pass unaffected through the Bragg grating. Since the frequency of the reflected light is proportional to the spacing of the Bragg grating, a change in the spacing will result in a change in the reflected wavelength. Hence, a strain gauge can be made by bonding a Bragg grating of a specific wavelength to a structure [8].

As the structure is strained, the Bragg grating will expand or contract, thereby changing the wavelength of the reflected light. By measuring the wavelength of the reflected light, one can deduce the strain at the location of the grating [8].

One major advantage of using fibre Bragg gratings as local strain sensors is the capability of using wavelength and/ or time division multiplexing to place many Bragg gratings, or strain sensors, along a single optical fibre. When a radiation source is used with a Bragg grating, every wavelength, except the wavelength corresponding to the grating, is transmitted through the grating. Therefore, a second Bragg grating, at a different wavelength, may be placed further along the fibre. This second Bragg grating will reflect a different wavelength back to the source. Now, two separate strain readings can be taken by monitoring the two reflected wavelengths. This process can be repeated many times along the length of the fibre, which allows making many distributed local strain readings within a single fibre-optic cable that also transmits all of the data back to the control computer. Similarly, time division multiplexing can be achieved by monitoring the time of return of the Bragg grating wavelengths, enabling interrogation of multiple sensors along a fibre [8].

One disadvantage of Bragg grating strain sensors is its strong thermal sensitivity, which is typically greater than that of the EFPI sensor [8].

2.2.3 Piezoeletric sensors

It is well known that piezoelectric elements have a wider dynamic range than resistive strain gauges. Therefore, they are applied to health monitoring that uses the high-frequency range. It is a great advantage that a piezoelectric element can act as an actuator because the health monitoring technique using piezoelectric actuators and sensors can be used to detect tensile or fatigue damage and impact damage [8].

Piezoelectric thin films such as Polyvinylidene Fluoride (PVDF) and Lead Zirconate Titanate (PZT) can be integrated into materials and structures due to their small size. PZT has better transmission efficiency and higher sensitivity than PVDF. However, due to its low stiffness and high flexibility, a thin PVDF film can be formed into any desired shape to be attached to the surface of complex structures. In most cases, piezoelectric sensors are distributed to monitor the overall region of materials and structures [8].

Health monitoring by piezoelectric elements can be classified into structural vibrational monitoring, impact damage monitoring, internal damage detection by diagnostic signals, structural impedance monitoring, and internal damage monitoring by Lamb wave, as shown in Figure 2.11 [8].

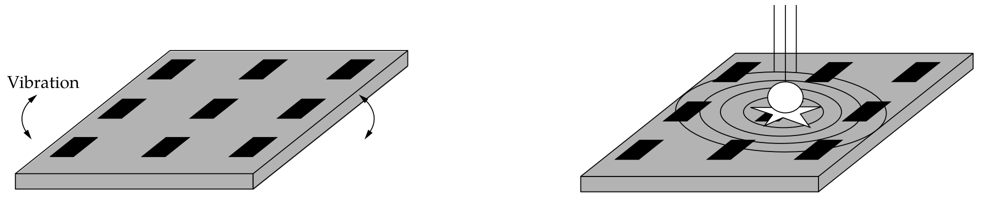

(a) Structural vibration (active or passive)

(b) Impact damage

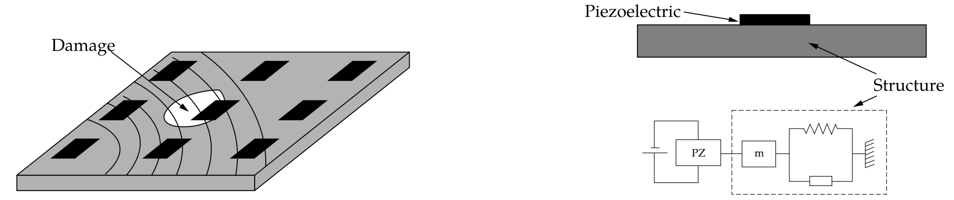

(c) Internal damage

(d) Impedance

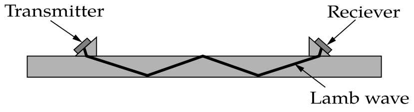

(e) Internal damage by Lamb wave

Figure 2.11: Intensity-based fibre optic monitoring configurations [8]

More recently, Pedro Ferreira et al. [3] have successfully incorporated piezoelectric particles into an AA5083-H111 plate using solid-state processing technology, thus creating a SSM. This topic will be discussed in more detail in Section 2.3 since this emerging technique represents a technological breakthrough in embedding sensors in metallic parts.

2.2.4 Shape memory alloys actuators

The SME is being studied to produce shape memory actuators that can generate mechanical work in response to temperature variations, which can be induced through changes in ambient temperature or by Joule's effect when a current is applied to the material. During the shape recovery phase, if an external action is applied to the shape memory alloy that opposes its recovery, then the recovery force and displacement will have the same direction. Thus, positive mechanical work is generated [23].

Many applications are currently being implemented in the aerospace, automotive, and biomedical industries. However, the main focus is replacing conventional servomechanical systems with SM-actuators. By so, it is expected to simplify the products reducing their mechanical complexity while improving their performance by reducing their size and weight. Additionally, SM-actuators do not require traditional transmission elements based on friction phenomena such as gears and therefore do not generate dust or any hazard regarding sparks. Another important aspect regards the vibration-free and quiet operation mode [23].

Regarding small size and weight actuators (< 100 g), depicted in Figure 2.12a, due to their high power-to-weight ratio, they are widely used for miniactuaction and microactuation, namely in the biomedical field [23].

In the aerospace and automotive industries, the application of SM-actuators is also currently limited to small-sized actuators since conventional ones outperform shape memory technologies in the range of medium and high-output strokes and forces [23].

Besides the size limitation described earlier, another aspect to consider is the low energy efficiency which depends highly on the configuration adopted and the type of deformation imposed. Also, the limited bandwidth for actuating derives mainly from the duration of the cooling phase since heating can be obtained quickly, as previously mentioned [23].

Regarding SM-actuators in the form of wires, depicted in Figure 2.12b, they can generate considerable force but with low useful stroke (3-5 %). When wound as helical springs, they provide higher strokes but at the expense of the output force [23].

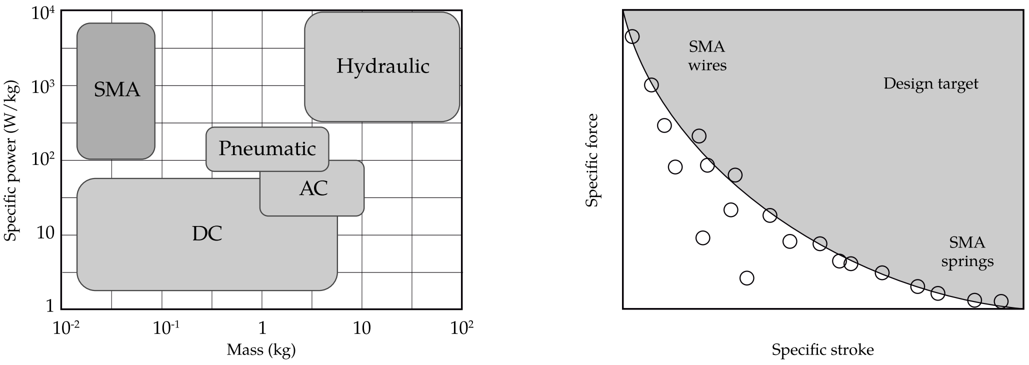

(a) (b)

Figure 2.12: Comparison of SMA actuators with alternative technologies in terms of specific power and overall mass (a); Typical behaviour of specific force versus specific stroke for SMA actuators (b) [23]

2.3 Application of smart materials in metallic parts

ESs are expected to aid in digital manufacturing techniques for Industry 4.0 that require in-process monitoring and control techniques to optimize production time and cost by enabling real-time information retrieval [11]. Furthermore, as stated in Section 1.1, ESs allow continuous monitoring of structures providing permanent records of the applied environmental conditions. Thus, ensuring improved safety and decreased costs [24]. FOSs and PSs are the most widely used technologies for developing ESs [2].

Although coupling between polymeric structural matrix and the sensors has been successfully achieved in many applications through direct embedment, metal matrix systems have required sensors to be externally attached to structures since internal embedment tends to involve high-temperature processes that damage the sensors [24].

Regarding the embedment of piezoelectric particles or thin films into a metal matrix, the maximum process temperature must not exceed the Curie temperature. Otherwise, it will lead to a breakdown or deterioration of their sensing performance. In addition, the high process temperatures may also inflict damage on the associated electronics and wire cladding [11].

Concerning the embedment of fibre optic materials, attempts have been made to use metal-based additive manufacturing and selective laser melting to embed FBG sensors. However, the residual stresses left by these processes tend to induce sensor damage along with poor coupling between the sensor and matrix [24].

Over the last two decades, efforts were made to cope with these constraints leading to the application of material-processing technologies that does not involve the fusion of base material, such as shape deposition manufacturing, layered manufacturing, laser deposited, and magnetron sputtering and electroplating [2]. More recently, solid-state processing such as Ultrasonic Additive Manufacturing (UAM) and Friction Stir Processing (FSP) have been studied and demonstrated to be very promissory in embedding FOSs and PSs.

Since these two emerging processing techniques demonstrate great potential in embedding sensors creating Metal Matrix Composites (MMCs), the following sections explain briefly both methodologies.

2.3.1 Ultrasonic addictive manufacturing

UAM is a solid-state processing technology invented in 1999 by Dawn White that derives from the solid-state ultrasonic welding process. It creates solid metal parts by ultrasonically joining a series of metal foils vertically. This process may be assisted by computerised numerical control machining to create internal features on the printed part or modify its external geometry [12].

This manufacturing process, depicted in Figure 2.13, uses an ultrasonic transducer to activate a sonotrode and induce high-frequency (ultrasonic) vibrations to scrub the metal foils while simultaneously exerting a compression force. Therefore, in this process, melting does not take place, and the joining mechanism is promoted by localized heat generation [12, 48]. The combination of high shear strain, normal pressure, and localized temperature increase has the effect of collapsing superficial asperities, scrubbing away the oxide layer, and promoting atomic diffusion from one material to another [24, 25]. Hence, this process allows the processing of similar and dissimilar materials [24].

Since this process does not involve melting, inert gas shielding and vacuum are not required. Another advantage is associated with the fact that the residual stress induced

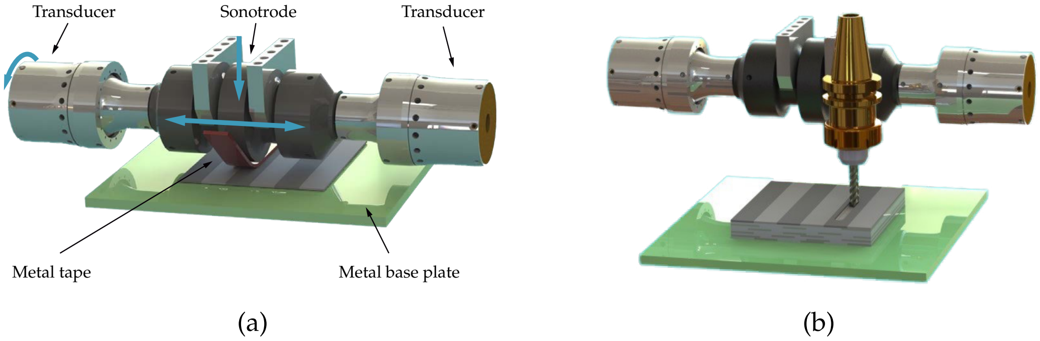

Figure 2.13: Embedding fibre optic strain sensors into metals using UAM: additive ultrasonic welding stage (a); subtractive computer numerical control machining stage (b) [48]

by this process is much lower compared with other addictive manufacturing techniques involving fusion [12].

Although the discussed advantages, this process has some limitations to consider. It is not suited for processing materials with high melting points and hardness since the working temperature cannot process such materials and the severe viscoplastic deformation involved. Another disadvantage regards not being able to manufacture parts with much geometric complexity due to high normal forces applied by the sonotrode [12].

Nevertheless, this emerging processing method has demonstrated much potential in fabricating smart metal components with fully ESs, actuators, and MEMSs [12].

2.3.2 Friction stir processing

FSP is a solid-state processing technology based on the viscoplastic stirring phenomena, which derives from solid-state Friction Stir Welding (FSW). It was proposed by Mishra in 1999, and since then, it has proven to be an energy-efficiency process, versatile, with low environmental impact and with the capacity to improve mechanical properties through grain refinement due to the dynamic recrystallization or by incorporating reinforcement materials into the metal matrix [3, 49].

Similarly to UAM, melting does not occur in this process, and the processing temperatures for aluminium alloys typically reach a temperature of 60% - 90% of the material's melting point [50]. Hence, the processing of dissimilar materials is also possible. Although this process is extensively used to create Functionally Graded Materials (FGMs), it has proven great potential to produce SSMs by incorporating piezoelectric particles [3].

The FSP principle, depicted in Figure 2.14, can be implemented on conventional FSW machines. The base metal is processed with a non-consumable rotating tool with a pin and a shoulder. During this process, the tool rotates at high speed and plunges into the workpiece under axial force until the shoulder contacts the surface. The tool then traverses relative to the workpiece along the process direction. The contact between the shoulder and the base material promotes localized heat generation through friction phenomena, which softens the processing region leading to severe plastic deformation [49].

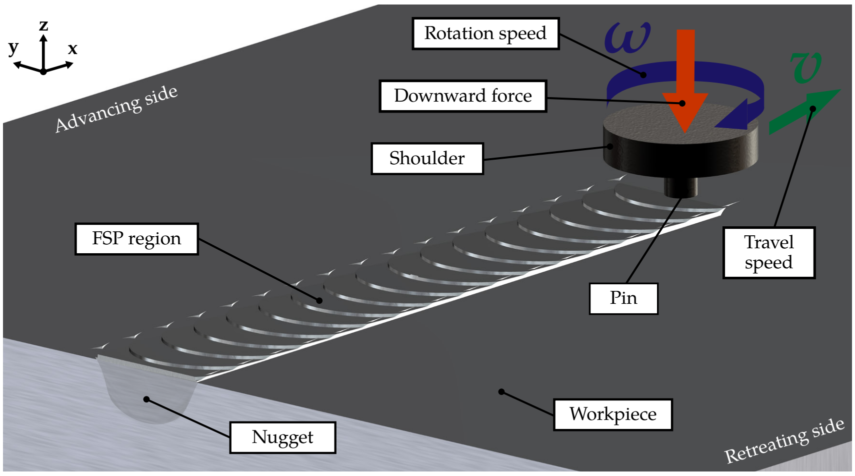

Figure 2.14: Representation of friction stir processing

2.3.3 Embedded fibre optic sensors

This section presents an in-depth review of the state-of-the-art regarding embedding FOSs in metallic parts, complementing the work carried out by Pedro Ferreira et al. [2].

Over the last couple of decades, much effort has been dedicated to developing new techniques to embed FOSs in metallic parts. Xiaochun Li et al. are among the main boosters using low-temperature processes to prevent damaging fibres, namely magnetron sputtering and electroplating and layered manufacturing. The research focuses on measuring temperature and strain on nickel and stainless steel structures, showing satisfactory results in terms of sensitivity when compared with unembedded sensors [34–37].

Alemohammad et al. [43] used a similar process to monitor a cutting tool subjected to thermal cycles achieving good results, although stress cycle monitoring should have also been considered.

Mou et al. [26], Li et al. [33], Schomer et al. [29, 38], Hehr et al. [27, 28, 42], Chilelli et al. [41], Petrie et al. [30], and Hyer et al. [31] demonstrated the feasibility of integrating FOSs using UAM processing technology to monitor temperature, strain, crack growth, and residual stress in aluminium and stainless steel parts.

Grandal et al. [39] and Jinachandran et al. [40] incorporated FOSs using different processing technologies showing promising results with identical thermal and strain sensitivities compared with the same unembedded sensors.

Embedding metal-coated fibres has proven to be an effective solution to guarantee the application of FOSs in high-temperature harsh environments. Using plated foils has also proven to increase bonding between layers in UAM [27, 30–33].

Table 2.3 presents a summarized overview of the developments made regarding the embedment of FOSs in metallic parts.

Table 2.3: Overview of applications and methodologies of integrating FOSs in metallic parts [2]

Author	**Methodology of integrating sensors**	**Measurements**	**Sensitivity**	**Applications**
Li et al. [34] (2000)	Magnetron sputtering and electroplating	Temperature	0.0245 nm/°C	Nickel an stainless steel structures
Li et al. [35] (2001)	Magnetron sputtering and electroplating	Temperature	0.021 nm/°C	Nickel an stainless steel structures
Li et al. [36] (2003)	Layered manufacturing	Temperature Strain	0.0334 nm/°C 1.245×10^{-3} nm/$\mu\varepsilon$	Monitoring the accumulation of residual strain
Li et al. [37] (2004)	Layered manufacturing	Temperature	-	Turbine blades and others' rotary metal tooling
Mou et al. [26] (2011)	Ultrasonic addictive manufacturing	Temperature Strain	36 pm/°C 0.1 nm/kg 0.73 nm/m^{-1}	Evaluation of sensing performance on AA3003-H18 and AA3003-O components
Alemohammad et al. [43] (2011)	Magnetron sputtering and electroplating	Temperature Residual stress	21 pm/°C	Metal cutting tools
Li et al. [33] (2012)	Ultrasonic addictive manufacturing	Temperature Strain	27.0-27.8 pm/°C 0.57-0.64 μm/N	Evaluation of sensing performance
Havermann et al. [32] (2015)	Selective laser melting	Temperature Strain	31.7 pm/°C 0.92 pm/$\mu\varepsilon$	Stainless steel SS316 components
Schomer et al. [29] (2016)	Ultrasonic addictive manufacturing	Temperature Strain	-	Evaluation of sensing performance on A6061
Schomer et al. [38] (2017)	Ultrasonic addictive manufacturing	Temperature	-	High-temperature environments
Grandal et al. [39] (2018)	Laser cladding technology	Temperature Strain	23-29 pm/°C 0.9-1 pm/$\mu\varepsilon$	High-temperature environments
Jinachandran et al. [40] (2018)	Metal packaging using stainless steel and tin	Temperature Strain	11.16 pm/°C 0.4456 $\mu\varepsilon$/N	Iron pipelines and ferromagnetic components
Hehr et al. [27] (2018)	Ultrasonic addictive manufacturing	Strain	-	Evaluation of strain sensing performance
Hehr et al. [28] (2019)	Ultrasonic addictive manufacturing	Strain	spatial resolution ≈ 1 mm	Fatigue testing on AA6061-T6 components
Chilelli et al. [41] (2019)	Ultrasonic addictive manufacturing	Cracks	Lenght of 0.286 ± 0.033 mm	Complex systems
Petrie et al. [30] (2019)	Ultrasonic addictive manufacturing	Strain	-	High-temperature environments
Hehr et al. [42] (2020)	Ultrasonic addictive manufacturing	Residual stress Temperature	-	Fibre-routing designs and alloy systems
Hyer et al. [31] (2022)	Ultrasonic addictive manufacturing	Temperature Strain	-	Stainless steel SS304 components in nuclear reactors

2.3.4 Embedded piezoelectric sensors

As previously discussed in Section 2.3, the embedment of PSs using traditional manufacturing processes imposes several adversities, such as high-temperatures and long curing times of the adhesives used to connect the sensor to the metal [2].

Over the last few years, much work has been done to resolve these challenges by adopting "stop and go" process methodologies or using solid-state manufacturing processes [2].

So far, the studies carried out proved the feasibility of embedding PVDFs and PZT sensors to evaluate strain, temperature, and impact detection with satisfactory sensitivities

[2, 3, 13–16].

Yanaseko et al. [13, 14, 21], Horikiri et al. [15], and Wang et al. [16] have contributed to the development of metal-core piezoelectric fibre embedded in aluminium metal matrix and its characterisation and electromechanical responses.

Ramanathan et al. [22] successfully used UAM to embed a piezoelectric PVDF into an aluminium metal matrix part measuring its response to strain.

More recently, Pedro Ferreira et al. [3, 44] used FSP to embed BTO particles in an aluminium metal matrix plate granting sensorial properties to it.

These solid-state processing technologies were first used to embed piezoelectric sensors and particles, revealing promising future employment results.

Table 2.4 presents a summarized overview of the developments made regarding the embedment of PSs in metallic parts.

Table 2.4: Overview of applications and methodologies of integrating PSs in metallic parts [2]

Author	**Methodology of integrating sensors**	**Measurements**	**Sensitivity**	**Applications**
Lin et al. [17] (2001)	Open contact-moulding process or others	Damage and material degradation	-	Metallic and composite structures
Yanaseko et al. [13] (2015)	Hot-pressing process	Strain	≈ 6.67 mV/$\mu\varepsilon$	Fabrication of metal matrix piezoelectric composite
Hossain et al. [18] (2016)	Electron beam melting	Stress	0.42-0.53 V/kN	Pressure tubes and turbine blades
Tseng et al. [19] (2018)	Casting	Temperature	0.37 °C/bit	Solid metal structural component
Altammar et al. [20] (2018)	Sandwich panel manufacturing	Wave propagation analysis (damage)	-	Laminate structures
Yanaseko et al. [21] (2019)	Hot-pressing process	Displacement	14.0 mV/μm	Evaluation of viscosity characteristics
Horikiri et al. [15] (2019)	Hot-pressing process	Output voltage	-	Fabrication of metal matrix piezoelectric composite
Yanaseko et al. [14] (2019)	Hot-pressing process	Output voltage	-	Impact detection
Wang et al. [16] (2020)	Hot-pressing process	Residual stress	-	Evaluate residual thermal stress during fabrication
Ramanathan et al. [22] (2021)	Ultrasonic addictive manufacturing	Strain	9.4 mV/$\mu\varepsilon$	Functionalised metal structures
Pedro Ferreira et al. [3] (2022)	Friction stir processing	Stress	12.0×10^{-4} μV/MPa	AA5083-H111 structural components

3

Experimental Methodology

This chapter comprehensively explains the experimental methodology employed to produce and characterise the SSMs. It covers the base materials' composition, the piezoelectric particles' characterisation, the equipment and tools utilised, the experimental setup, and the measurements taken to monitor the material processing. Additionally, it explains the various characterisation techniques employed to assess the mechanical and sensorial behaviour of the SSMs.

3.1 Characterisation of base material

As discussed in Section 1.2, to grant sensorial properties to the heat-treated AA2017-T451 and AA7075-T651 plates, PZT and BTO particles were incorporated using FSP.

To achieve these tempers, the plates were subjected to a solution heat treatment, followed by a stress-relieving process through controlled stretching (1.5% and 3% for plates) and then were naturally or artificially aged, according to T451 or T651 tempers, respectively [51].

The nominal chemical compositions of the AA2017-T451 and AA7075-T651 plates are presented in Tables 3.1 and 3.2, respectively.

Table 3.1: AA2017-T451 plates' chemical composition (wt%) [45]

Elements	Si	Fe	Cu	Mn	Mg	Cr	Zn	Ti+Zr	Al
Min	0.2	-	3.5	0.4	0.4	-	-	-	-
Max	0.8	0.7	4.5	1	1	0.1	0.25	0.25	Remaining

Table 3.2: AA7075-T651 plates' chemical composition (wt%) [46]

Elements	Si	Fe	Cu	Mn	Mg	Cr	Zn	Ti	Al
Min	-	-	1.2	-	2.1	0.18	5.1	-	-
Max	0.4	0.5	2	0.3	2.9	0.28	6.1	0.2	Remaining

The principal alloying element in AA2017-T451 is copper (Cu), whereas in AA7075-T651, magnesium (Mg) and zinc (Zn) serve as the primary alloying constituents. These particular elements are conventionally integrated into 2xxx and 7xxx aluminium alloys, respectively, to enhance mechanical strength and facilitate precipitation hardening.

The dimensions of the AA2017-T451 and AA7075-T651 aluminium plates used to manufacture the SSMs are 203 (rolling direction) × 103 × 8 mm and 203 (rolling direction) × 103 × 10 mm, respectively. Both materials' mechanical and physical properties are listed in Table 3.3 [45, 46].

Table 3.3: Mechanical and physical properties of AA2017-T451 and AA7075-T651 plates [45, 46]

Mechanical and physical properties	**Yield strength, $\sigma_{0.2}$ [MPa]***	**Modulus of elasticity, E [GPa]**	**Ultimate tensile strength, σ_{UTS} [MPa]***	**Brinell hardness [HB]**
AA2017-T451	260	72	390	111
AA7075-T651	460	71	540	160

*Minimum values

3.2 Characterisation of piezoelectric particles

As previously stated, to grant sensorial properties to the aluminium base material, BTO and PZT piezoelectric particles were incorporated.

A physicochemical characterisation of the BTO particles ($BaTiO_3$) is depicted in Figure 3.1, revealing the morphology and size of these particles, and their elemental chemical composition.

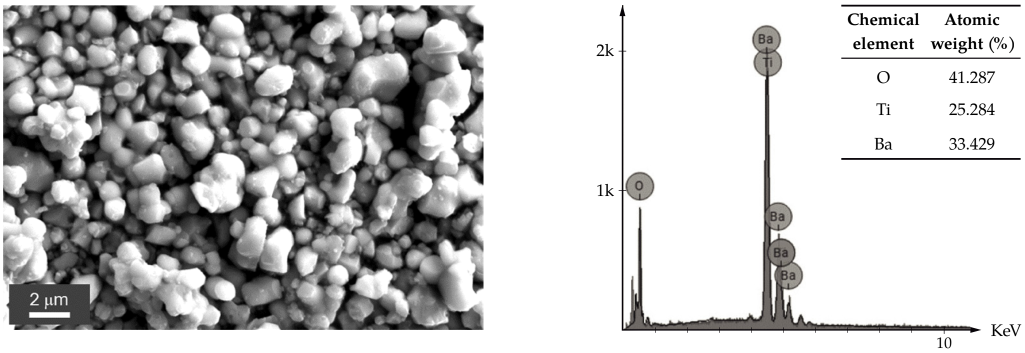

(a)

(b)

Figure 3.1: Physicochemical characterisation of BTO particles: scanning electron microscopy (SEM) image (a); chemical elemental mapping determined by energy-dispersive X-ray (EDX) spectroscopy (b) [3, 44]

These particles have a purity of 99.7% and present a homogeneous granular morphology with a grain size approximately smaller than 2 μm. The energy-dispersive X-ray spectroscopy analysis revealed the presence of oxygen (O), titanium (Ti) and barium (Ba) as expected.

A similar analysis was conducted on the PZT particles ($PbZr_{0.52}Ti_{0.48}O_3$) to characterise their morphology and size, as presented in Figure 3.2.

These particles have a purity of 99.9%, and their size ranges from sub-micron dimensions to approximately 20 μm. Contrastingly to the BTO particles, these tend to form

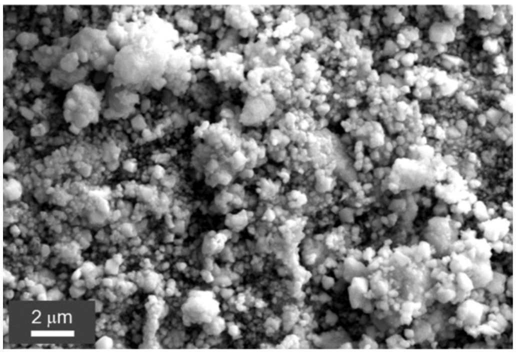

Figure 3.2: Characterisation of PZT particles: scanning electron microscopy (SEM) image [44]

agglomerates of particles, as evidenced in Figure 3.2. The PZT particles were produced from a solid solution of 52% lead zirconate and 48% lead titanate [44].

Both SEM images of BTO and PZT were obtained through an analysis with a compact scanning electron microscope ZEISS Merlin VP. A thin coating of conductive gold with 6 nm was added to improve the particles' conductivity using the sputtering technique [3, 44]. These particles are commercially available and were manufactured by Alfa Aesar [52] and Nanoshel Ltd. [53], respectively.

BTO and PZT particles are piezoelectric ceramics containing numerous microscopic ferroelectric crystals. These crystals exhibit a perovskite crystalline structure, which can assume tetragonal, rhombohedral, orthorhombic, or simple cubic phases depending on the subjected temperature, referred to as the Curie temperature, T_c.

Below the Curie temperature, $BaTiO_3$ transforms successively to three ferroelectric phases: tetragonal, orthorhombic and rhombohedral. These phases have spontaneous polarisation directions, [001], [011], and [111], respectively, due to the asymmetric arrangement of the lattice structure and, therefore, have an electrical dipole. Similarly, $PbZr_xTi_{1-x}O_3$ typically presents tetragonal or rhombohedral phases below this temperature, exhibiting spontaneous polarisation. However, the exact phase depends on the specific composition of the material [54].

Above the Curie temperature, $BaTiO_3$ and $PbZr_xTi_{1-x}O_3$ lose the spontaneous polarisation given the more symmetric lattice structure [44].

The presence of an electrical dipole within the crystalline structure causes deformation in response to an electric field (converse piezoelectric effect) or generates electrical displacement when subjected to mechanical strain (direct piezoelectric effect). The manifestation of mechanical strain or variation in the electric dipole does not necessarily yield observable effects at the macroscopic level. This is because the dipoles arrange themselves into domains randomly distributed within the polycrystalline material. To achieve macroscopic manifestations, a preferential orientation of these domains, known as polarisation, is required [3].

The piezoelectric and physical properties of BTO and PZT piezoelectric particles are presented in Table 3.4 for comparative purposes [44].

Table 3.4: Piezoelectric and physical properties of $BaTiO_3$ and $PbTiZrO_5$ [44]

Piezoelectric and physical properties	**$BaTiO_3$**	**$PbTiZrO_5$**
Dielectric constant (K_{33})	1700	1300
Piezoelectric constant (d_{33}, d_{31}) [pC/N]	190, -78	270, -120
Electromechanical coupling coefficient (k_{33}, k_{31})	0.50, 0.21	0.71, -0.34
Curie temperature (T_c) [°C]	115	300-370
Density (d) [g/cm^3]	6.08	7.70

3.3 Production of the self-sensing materials

3.3.1 Milling machine and tools

The piezoelectric particles were embedded into the aluminium through FSP. The three-axis milling machine used to produce the SSM is depicted in Figure 3.3.

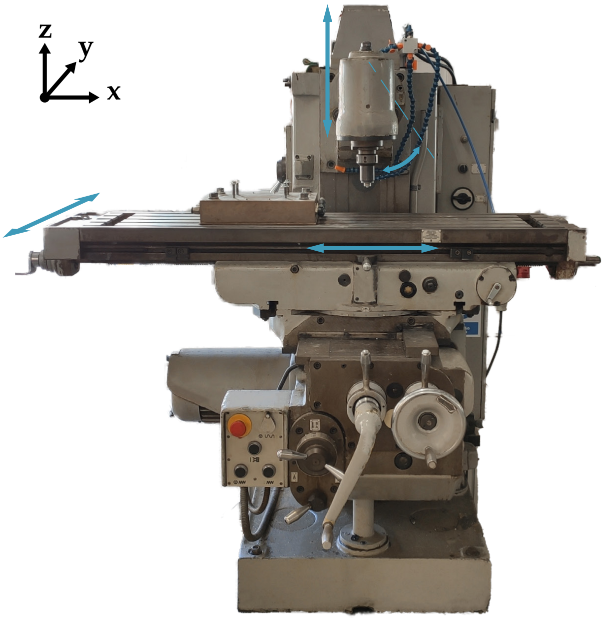

Figure 3.3: Three-axis milling machine

The set of tools is presented in Figure 3.4, and it is composed of a left-handed scrolled shoulder without a pin (pinless FSP tool) and a featureless concave shoulder with a triflute left-handed conical pin (pinned FSP tool). The selection of the pinned FSP tool was based on the research conducted by Inácio et al. [55] and Vidal et al. [56] and guarantees an optimal distribution of particles. Both pinless and pinned tool's shoulders have a diameter of 19 mm. The pin has a conical geometry with 14° and a bottom diameter of 5 mm. All tools were made of H13 steel [3].

The process parameters for incorporating these particles are already established and optimized according to the work developed by Pedro Ferreira et al. [3]. Nevertheless,

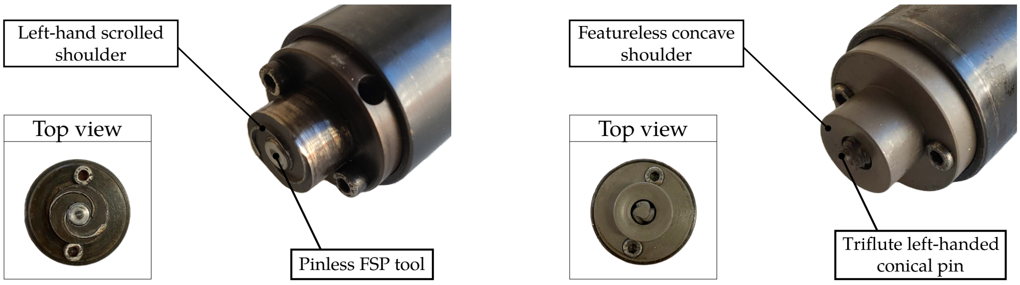

(a) (b)

Figure 3.4: FSP tools: pinless tool (a); pinned tool (b)

these parameters represent only a starting point since the processed base material differs from that used in [3]. To avoid the formation of defects and ensure the best particles' distribution, adjustment of these parameters shall be considered to process the AA2017 and AA7075 plates.

Similarly to the procedure adopted in [3], three steps are considered to embed the piezoelectric particles into the plates, as presented in Figure 3.5. First, the piezoelectric particles are placed and compacted into a single groove previously machined by milling. Then, a single-pass is performed with the pinless FSP tool to close the groove and confine the particles. Finally, four passes are performed with the pinned tool in the same direction (X-direction), without any offset in the transverse direction (Y-direction), to ensure greater distribution and homogeneity of the particles along with the nugget [3].

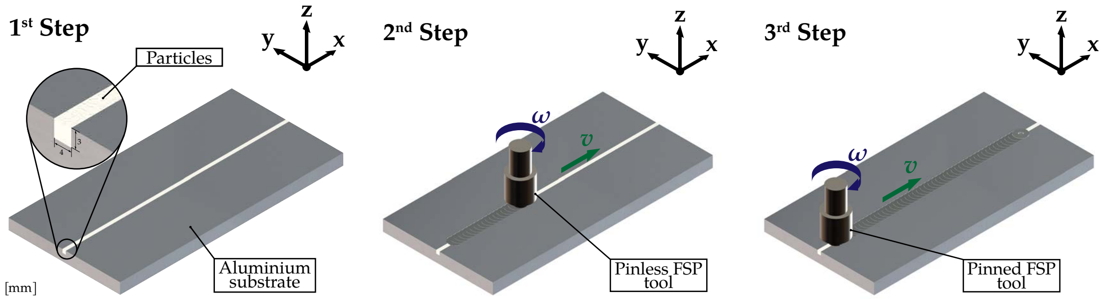

(a) (b) (c)

Figure 3.5: Steps performed to embed the particles in the metal plate: particles compaction in the groove (a); single pass with the pinless FSP tool to close the groove (b); four passes with the pinned FSP tool to stir the material (c)

3.3.2 Temperature measurements

During the processing of the plates, the temperature evolution was recorded using six equally spaced K-type thermocouples along the length of the plate, as illustrated in Figure 3.6. The odd indices (T-K1, T-K3, T-K5) are referred to as the retreating side (RS), while even indices (T-K0, T-K2, T-K4) regard the advancing side (AS). In order to accommodate the thermocouples and ensure optimal contact between them and the plates during their processing, six grooves were previously machined.

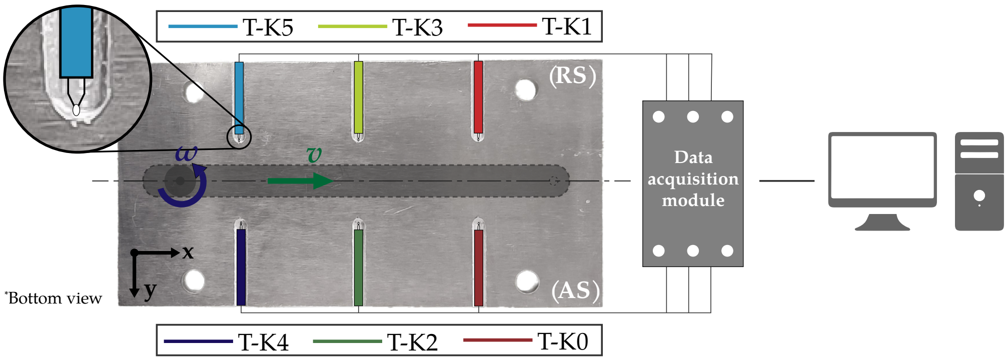

Figure 3.6: Thermocouples' distribution along the plate

Kapton tape was used to secure the thermocouples from moving during the processing of the plates. The temperature data acquisition was made using the NI 9213 input module, installed in the NI-cDAQ-9178 CompactDAQ chassis from National Instruments. The data processing and recording were performed using LabView 2015 software.

Additionally, the surface temperature of the plates was recorded during its processing using a Fluke Ti400 infrared thermal camera. This equipment has a thermal sensitivity of 0.05 °C and an accuracy of 2 °C.

The top surfaces of the plates were painted black to prevent the reflection of infrared radiation emitted by the surroundings, allowing for a more precise measurement of the temperatures involved during processing. The camera's emissivity was set to 0.95 for accurate temperature readings.

3.3.3 Polarisation process

Establishing a preferential orientation of the randomly arranged piezoelectric particles' electrical dipoles is necessary after processing to achieve a macroscopic electrical effect. Thus, a polarisation process is performed by applying a strong electrical field (9 kV/mm) in a controlled environment at a temperature of 90°C. This process ensures an asymmetry in the previously disorganized compound [3]. The electrical field (DC) is generated using an Oficel adjustable voltage generator. To regulate the temperature at which the polarisation is carried out, a digital-control power supply RS-3005D was used.

Applying a strong electrical field causes a reorientation of the spontaneous polarisation previously introduced while processing the material. Simultaneously, domains aligned favourably with the polarity field direction grow, while those aligned unfavourably shrink. Following polarisation, the induced preferential orientation is retained even though the electrical field is no longer applied. Nevertheless, a small number of domain walls may return to their original positions due to internal mechanical stresses [3].

This procedure, depicted in Figure 3.7, has proven to be very effective in increasing the electrical response of the SSM [3].

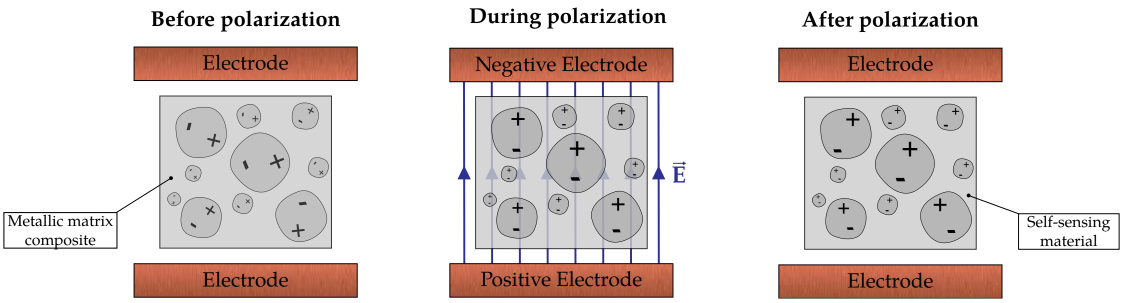

Figure 3.7: Schematic of polarisation process

3.4 Characterisation of self-sensing materials

This section addresses the different characterisation techniques employed to evaluate the mechanical and sensorial properties of the produced SSMs. Figure 3.8 presents a schematic illustration of the samples used in each characterisation technique and their location inside the produced plate for a better understanding of further subjects, including the discussion of results.

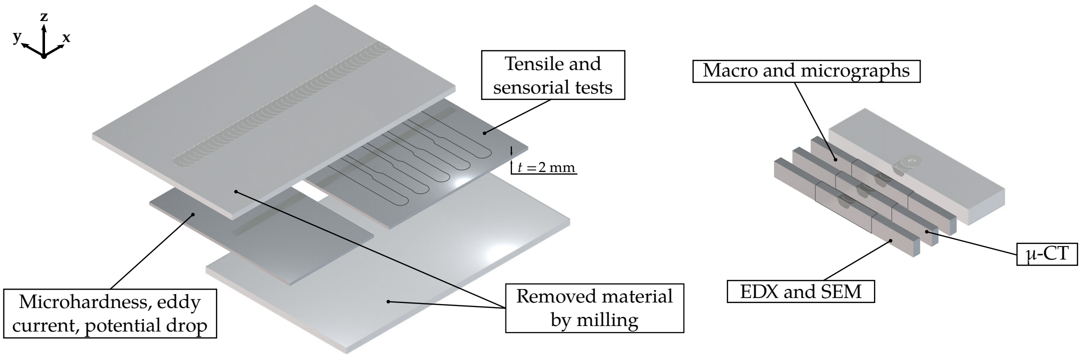

Figure 3.8: Schematic illustration of the samples and their location inside the SSMs' plates for the various characterisation techniques

3.4.1 Metallographic characterisation

In order to examine the macrostructure and particles' distribution, a comprehensive macrostructural analysis was conducted on the SSMs using an Olympus CX40 optical microscope. The macrographs were assembled with the Adobe Lightroom 2023 photo merge tool from multiple micrographs taken with the 5x magnification lens.

All samples were embedded in epoxy resin, carefully grounded, and polished following standardized metallographic procedures. A Keller's reagent solution was used to etch the samples with the below chemical composition.

- Distilled water - 175 ml
- Hydrochloric acid (HCl) - 3 ml (37%)
- Nitric acid (HNO_3) - 20 ml (65%)
- Hydrofluoric acid (HF) - 2 ml (48%)

Additionally, particular attention was given to examine and characterise the microstructure and particles' distribution at key macrostructural regions, namely the nugget area where the piezoelectric particles were embedded, using the inverted microscope Leica DMI 5000 M, at the Materials Research Center of NOVA SST - CENIMAT-i3N.

The macrographs were used to guide the selection of the locations for EDX measurements. The SEM and EDX analyses were conducted with a Zeiss Merlin VP compact SEM equipped with a Bruker XFlash EDX detector at Aalto University, Finland. The specimens were mounted in a bakelite thermosetting resin with carbon filler, appropriate for examination in a SEM, and prepared using a Struers Tegramin automatic polisher with a final grinding with a 1200 grit paper. A final polishing with 1 μm and then 25 μm diamond suspension was conducted. The acceleration voltage and working distance were 15 kV and $\approx$ 12 mm, respectively.

3.4.2 Microcomputed tomography characterisation

The samples' 3D micro-architectural morphology was assessed using X-ray microtomography (µCT) with a Phoenix V | TOME | X, GE system, following the procedure outlined by Vidal et al. [56]. The obtained image data were subjected to qualitative and quantitative interpretation utilizing 3D tomographic reconstruction and analysis software, Volume Graphics 3.04 software [3].

3.4.3 Uniaxial tensile tests

Uniaxial tensile tests were conducted at ambient temperature using a servo-hydraulic MTS 312.21 testing machine equipped with a load capacity of 100 kN, following the ASTM E8/E8M-13a standard. A HAAS Super Mini Mill 2 CNC Machining Center was employed to prepare the specimens for testing, with the geometry depicted in Figure 3.9. All specimens were carefully machined with a uniform thickness, t, of 2 mm, measured from the bottom part of the nugget, ensuring accessibility to both sides of the nugget. The fracture surface was analysed by a SEM Hitachi High-Tech SU3800.

The uniaxial tensile tests assessed and characterised the SSMs' mechanical behaviour.

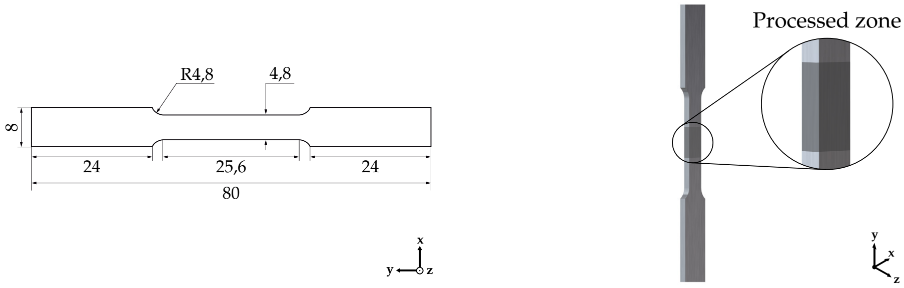

(a) (b)

Figure 3.9: Uniaxial tensile test specimen: technical drawing [mm] (a); processed zone closeup (b)

3.4.4 Microhardness measurements

The specimens were carefully prepared for this analysis, and the Vickers microhardness profile was obtained along its length (Y direction) utilizing a Mitutoyo HM-112 microhardness testing machine. The experimental procedure was performed on the upper surface of the plates, represented in Figure 3.8, and follows the ASTM E384 - 10 standards.

The spacing between consecutive indentations was set at 1 mm for the base material and reduced to 0.5 mm for regions affected by processing and thermal/mechanical influences. A standardized load of 1.0 kgf was applied for 10 seconds during the microhardness tests.

The microhardness measurements were carried out to characterise both the samples' processed and non-processed zones and assess the distribution of particles within the SSMs.

3.4.5 Electrical conductivity measurements

The electrical conductivity of the samples described in Section 3.4.4 was determined using eddy currents and potential drop measurement techniques, following the procedures developed by Sorger et al. [57] and Santos et al. [58]. These measurements were conducted along a straight line in the Y direction, next to the microhardness measurements.

For the eddy currents technique, a pencil probe operating at a frequency of 1.0 MHz was utilized in conjunction with a NORTEC 600 D impedance analyzer.

Potential drop measurements were performed using a standard Jandel linear four-point probe consisting of four tungsten needles aligned in a straight line configuration, each with a radius of 0.4 µm and 0.635 mm spacing between each other. An external current of 80 mA was applied to the outer needles using a Keithley SourceMeter 2450, while a Keithley Nanovoltmeter 2182A was employed to measure the voltage between the two inner needles, allowing the calculation of the electrical conductivity.

3.4.6 Sensorial properties assessment

To demonstrate the material's inherent self-sensing capabilities attributed to the presence of piezoelectric particles, a series of laboratory tests were conducted to evaluate its electrical response under dynamic solicitations [3]. An MTS 312.21 testing machine was employed to apply dynamic loads. The test specimens used for this analysis were uniaxial tensile test specimens, as depicted in Figure 3.10. Each uniaxial tensile specimen underwent dynamic loading, consisting of a load spectrum comprising fifteen tensile cycles at successive higher frequencies, f, 0.063, 0.125, 0.250, and 0.500 Hz. A range of different dynamic load intensities were applied. The load intensity was controlled by displacement (X direction), with amplitudes, A, set at 0.02, 0.03, 0.04, 0.05, 0.06, 0.07, 0.08, 0.09, and 0.10 mm.

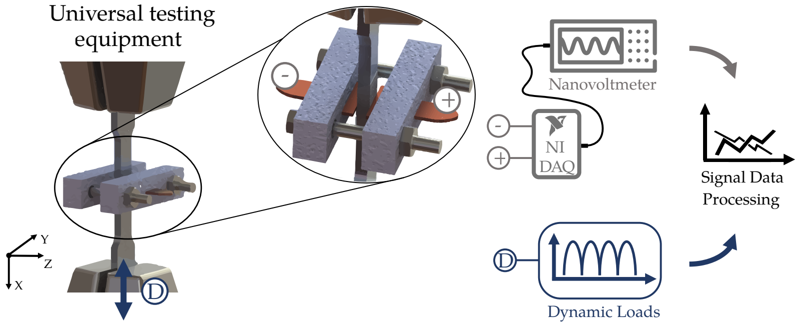

Figure 3.10: Experimental setup used to analyse the dynamic response of the SSM

For data acquisition, a load cell was utilized to measure the force induced by the dynamic loads. An electrical connection was established between the sample and the monitoring system, enabling direct contact with the sample surface, as illustrated in Figure 3.10. The copper electrodes were connected to a National Instruments 781325-01 myDAQ system's analog input port. The analog input has a maximum sampling rate of 200 kS/s per channel and can measure up to ±10 V signals. The National Instruments myDAQ system was connected to a Keithley Nanovoltmeter 2182A to measure the electrical voltage response, supported by a LabView program for signal data processing. The analog output of the nanovoltmeter provides a scaled, non-inverting voltage output up to ±1.2 V and can be calculated using Equation 3.1.

$$Analog\ output = Gain \times \frac{Rdg}{Rng} - Offset \tag{3.1}$$

where:
$Gain$ = user entered gain factor
Rdg = reading on the Model 2182
Rng = measurement range
$Offset$ = user entered offset value

The gain factor and the measurement range were set at 9000 and 0.01 V, respectively, and no offset was used. All testing procedures were conducted at room temperature.

4

EXPERIMENTAL RESULTS

4.1 Processing parameters optimization

Although the optimization of processing parameters has already been studied in the work conducted by Pedro Ferreira et al. [3], and the parameters are well-established for the AA5083-H111 alloy, it was necessary to determine the optimal processing parameters for the AA2017-T451 and AA7075-T651 alloys.

To accomplish this, the travel speed, v, was varied at 71, 90, and 112 mm/min while keeping the rotation speed, ω, constant at 1120 rev/min. The cross-sectional macrographs obtained for the processed regions of the AA2017 and AA7075 alloys are presented in Tables 4.1 and 4.2, respectively.

Table 4.1: Processing parameters optimization for AA2017-T451

	1st Pass	**2nd Pass**	**3rd Pass**	**4th Pass**
$v = 71$ mm · min^{-1} **$\omega = 1200$ rev/min**	-			
$v = 90$ mm · min^{-1} **$\omega = 1200$ rev/min**	-		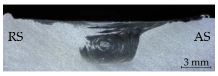	
$v = 112$ mm · min^{-1} **$\omega = 1200$ rev/min**	- 			

Table 4.2: Processing parameters optimization for AA7075-T451

	1st Pass	**2nd Pass**	**3rd Pass**	**4th Pass**
$v = 71$ mm · min^{-1} **$\omega = 1200$ rev/min**	-			
$v = 90$ mm · min^{-1} **$\omega = 1200$ rev/min**	-			
$v = 112$ mm · min^{-1} **$\omega = 1200$ rev/min**	- 		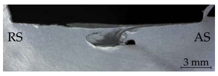	

After careful observation of the cross-section of the processed regions, defects with a very characteristic linear morphology can be noticed in the bottom section of the nugget, on the advancing side. However, these defects were not introduced by the process but rather resulted from misalignment between the tool pin and the groove machined in the plate.

Based on the obtained results regarding the surface quality of the processed region, the distribution of particles within the nugget, and the occurrence of defects during processing, the optimal parameters for distributing the particles have been determined to be v = 71 mm/min and ω = 1120 rev/min for AA2017, and v = 90 mm/min and ω = 1120 rev/min for AA7075.

Regarding the parameters to close the groove, it has proven to be optimal v = 71 mm/min and ω = 1120 rev/min for AA2017 and v = 90 mm/min and ω = 1400 rev/min for AA7075.

The Table 4.3 summarizes the processing parameters of the plates.

Table 4.3: Processing parameters employed for SSMs' production

Alloy	**Processing parameters**	**Groove closing**	**1^{st} - 4^{th} Passes**
AA2017-T451	Rotation speed, ω [rev/min]	1120	1120
	Travel speed, v [mm/min]	71	71
	Tilt angle, [°]	1	1
AA7075-T651	Rotation speed, ω [rev/min]	1400	1120
	Travel speed, v [mm/min]	90	90
	Tilt angle, [°]	1	1

4.2 Production of the self-sensing materials

The production of the SSMs follows the procedures outlined in Section 3.3. It is intended to process both piezoelectric particles, i.e., BTO and PZT, for each alloy, i.e., AA2017 and AA7075. In order to perform all the characterisation techniques stated in Section 3.4, two plates for each type of piezoelectric particles and each alloy were produced. Additionally, two plates without particles were processed, one for each alloy, to serve as a reference and evaluate the impact of adding the particles.

Henceforth, the following nomenclature was adopted whenever there is a need to differentiate the processed plates: [Alloy]-[Piezoelectric particles][Nr. of processed plate]. For example, AA2017-BTO1 refers to the first processed plate with BTO particles in the AA2017 alloy. On the other hand, the two processed plates without particles are denoted simply as AA2017-R and AA7075-R. When presenting the experimental results, whenever the nomenclature does not specify the processed plate number, it means that the average of the data was considered.

Figure 4.1 presents the production of the AA2017-BTO1 plate during the first pass processing.

The refrigerant fluid was employed exclusively between passes to minimize the waiting period required for the plate to cool down to room temperature.

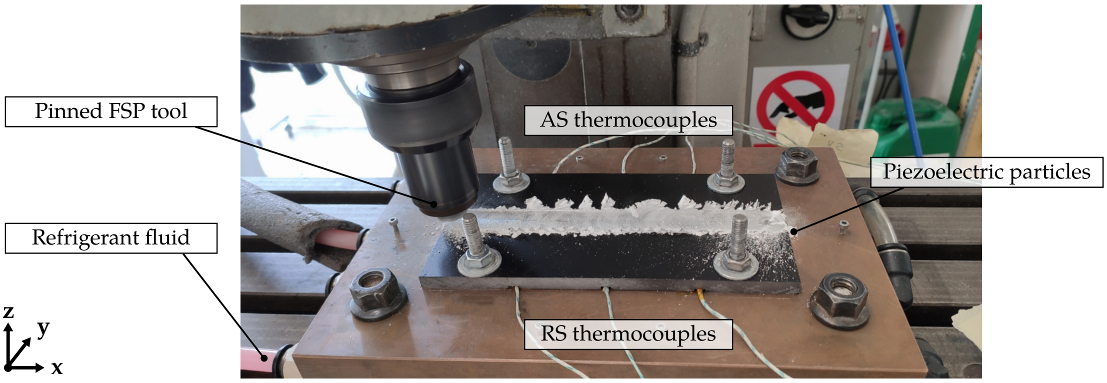

Figure 4.1: Production of SSM - 1st pass on AA2017-BTO1 plate

4.2.1 Temperature measurements

Figure 4.2 displays the typical temperature evolution during a processing pass and the thermocouples' measurements during the third pass of the 7075-PZT1 plate. As expected, the right-sided (X-direction) thermocouples register successively higher temperature values since the FSP tool contributed to the global heating of the plate in an immediate prior instance. It can also be inferred that the temperature on the AS is higher than on the RS, as anticipated [59].

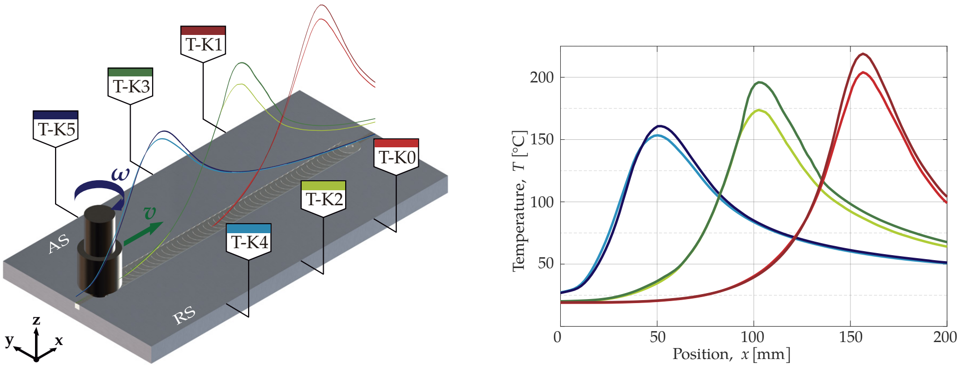

(a)

(b)

Figure 4.2: Temperature evolution during processing: schematic thermocouples' distribution (a); temperature measurements during third pass of AA7075-PZT1 (b)

The maximum temperatures registered by the thermocouples at the AS and RS during each pass while processing the SSMs and the plates without the piezoelectric particles are presented in Figure 4.3.

It is noticeable that peak processing temperatures in the AA2017 alloy were slightly higher than those recorded in the AA7075 alloy. This difference can be primarily attributed to the processing parameters used, as the AA2017 alloy was processed with $v = 71$ mm/min, while the AA7075 alloy was processed with $v = 90$ mm/min, both at the same rotational speed, resulting in a greater heat input in the first one.

For the same base material, using different embedding piezoelectric particles does

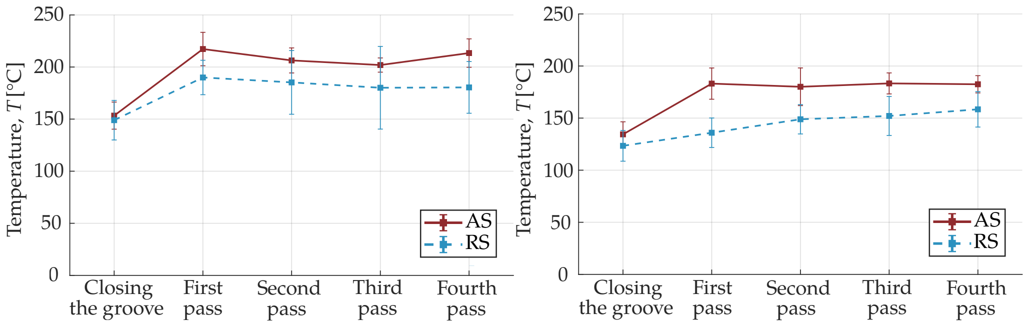

(a) AA2017-BTO (b) AA7075-BTO

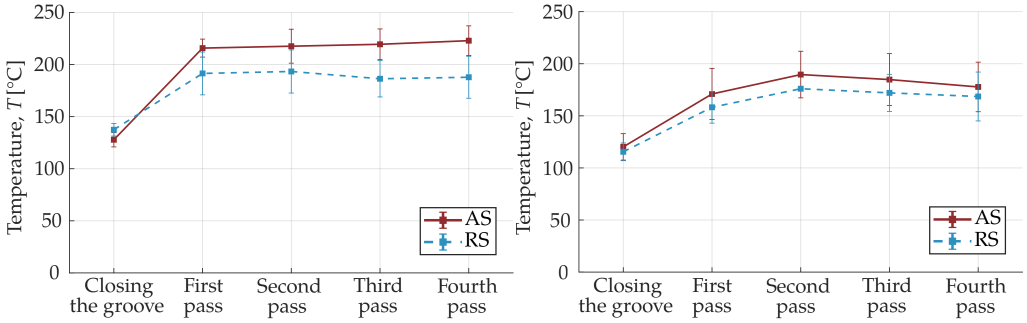

(c) AA2017-PZT (d) AA7075-PZT

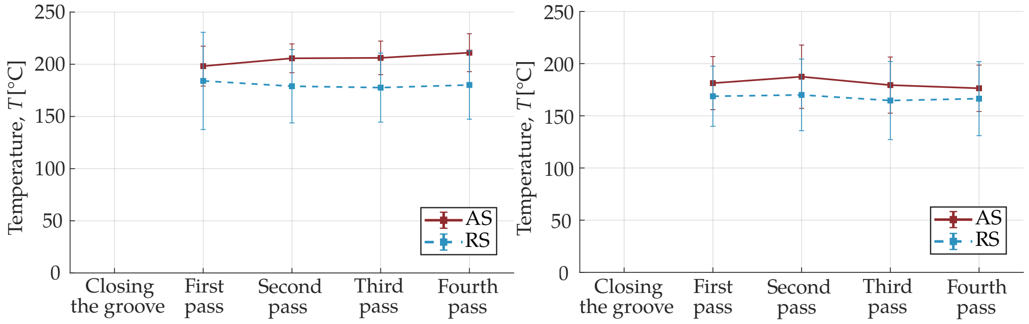

(e) AA2017-R (f) AA7075-R

Figure 4.3: Maximum temperatures of each pass registered by the thermocouples

not yield notable differences in the maximum temperature, as reported by Ferreira et al. [44]. However, when comparing the processing of the plates without the particles to the processing with the particles, it is evident that the recorded maximum temperatures are slightly higher in the latter case. Nevertheless, this disparity is more pronounced in the AA2017 alloy than in the AA7075 alloy.

The presented data above are merely representative of the temperature evolution during the plate processing and do not accurately depict the temperature reached in the nugget region. To attend this, the maximum temperature reached at the surface of the stir zone was recorded by thermal imaging camera during each plate processing pass, as depicted in Figure 4.4.

The recorded temperatures are higher than those obtained from the thermocouples.

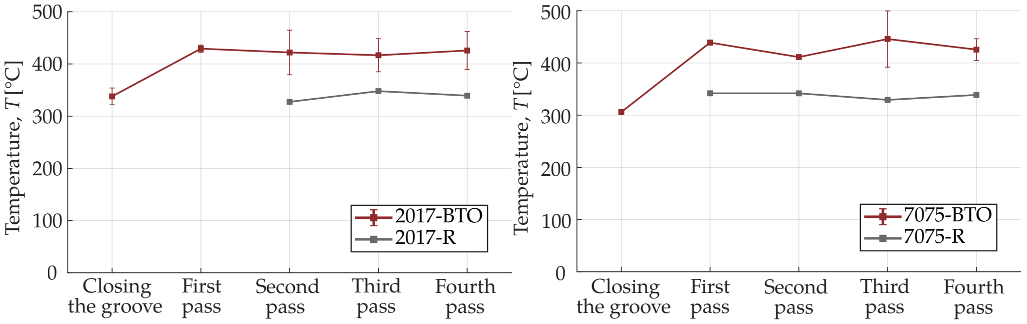

(a) AA2017-BTO (b) AA7075-BTO

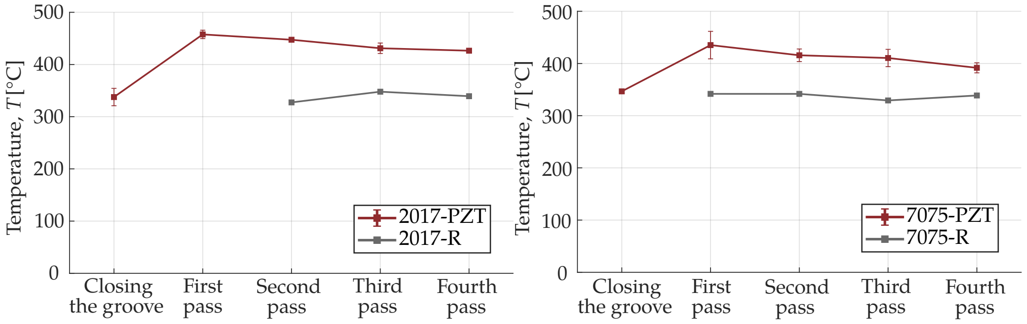

(c) AA2017-PZT (d) AA7075-PZT

Figure 4.4: Maximum temperatures of each pass registered by the thermal camera, at the surface of the stir zone

This result was expected, as the thermocouples are distributed and positioned below the plate, while the thermal camera directly measures the temperature in the stir zone.

Unlike the data collected from the thermocouples, these observations do not clearly evidence higher peak processing temperatures in the stir zone for the AA2017 compared to the AA7075. This is not completely unexpected since the process of embedding the piezoelectric particles is manual, which implies that the downward force is regularly being adjusted to compensate for minor misalignments of the FSP milling machine. This can cause sudden increases in temperatures, as shown in Figure 4.5.

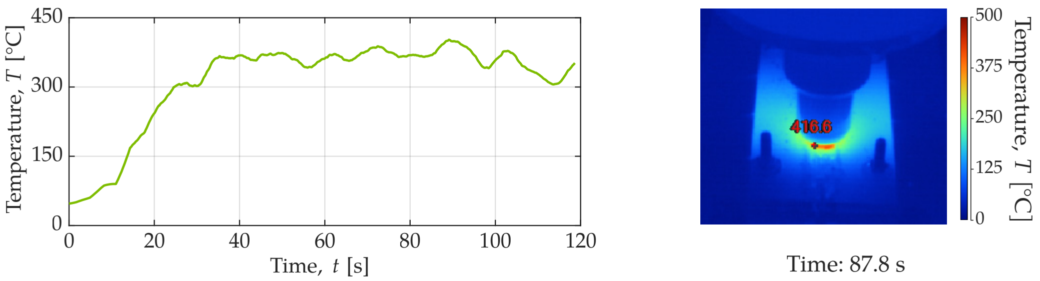

(a) (b)

Figure 4.5: Effect of manual adjustment of the downward force on AA7075-PZT2 plate: evolution of temperature during 1st pass (a); thermogram at maximum temperature (b)

The results obtained from the thermocouples and the thermal imaging camera evidence significantly lower temperatures closing the groove than in the subsequent processing passes. This is because the plastic deformation induced by the pinless FSP tool is significantly less compared to the pinned FSP tool, resulting in lower temperature generation.

Furthermore, it can be inferred that the number of passes does not influence the processing temperature, as the maximum temperature during the four processing passes remains approximately constant.

When comparing the maximum temperatures recorded by both the thermocouples and the thermal imaging camera for the plate processing situation, without and with particles, it is evident that temperatures increase, as expected. Incorporating particles in the processing matrix adds complexity, requiring more energy to disperse and embed them effectively. Also, adding ceramic particles to the aluminium matrix acts as an obstacle to the process's thermal flow, leading to increased local temperature due to its low thermal conductivity. Consequently, higher temperatures are observed during the processing with particles, which indicates increased energy dissipation and greater resistance to deformation.

4.2.2 Polarisation process

As discussed in Section 3.3.3, the SSMs were subjected to a polarisation process depicted in Figure 4.6 to achieve an enhanced macroscopic electrical response during dynamic solicitations.

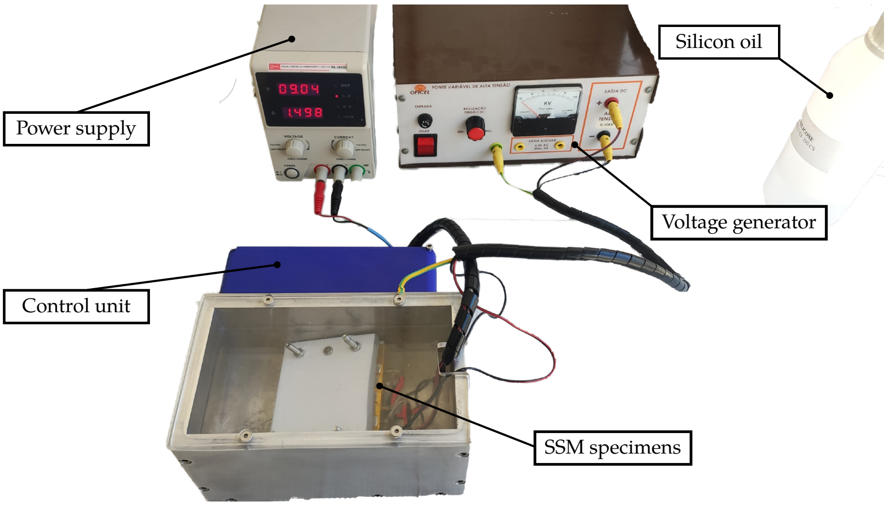

Figure 4.6: Experimental setup of the polarisation process

The uniaxial tensile specimens were submerged in silicon oil to reduce the risk of electrical breakdown due to its excellent dielectric properties, which makes it an excellent insulator.

The temperature was set at approximately 90 °C to increase the mobility of the domain walls, thus making it easier for the dipoles to reorient and stabilize in a preferential direction imposed by the electric field. Also, increasing the temperature helps reduce residual stresses that may have developed during the material's processing.

Even though higher temperatures are proven to facilitate the polarisation process for the reasons described above, increasing the temperature above 90 °C would be critical since it would be too close to the Curie temperature of BTO particles. As discussed in Section 3.2, if the temperature during polarisation surpasses the Curie temperature, the SSM loses its spontaneous polarisation, compromising the self-sensing properties. Hence, a control unit was employed to prevent the temperature from exceeding 90 °C.

4.3 Characterisation of self-sensing materials

4.3.1 Metallographic characterisation

The analysis of particle distribution inside the processed zone, i.e., the nugget, and the identification of other key microstructural regions, such as the heat-affected zone (HAZ) and the thermo-mechanically affected zone (TMAZ), were accomplished using macro and microstructural characterisation techniques. Figures 4.7 and 4.8 a-d present the macro and micrographs of the AA2017 and AA7075 SSM samples, respectively.

It can be noticed that FSP was able to successfully promote the distribution of the particles in both aluminium matrix alloys. Previous EDX analysis performed by Ferreira et al. [44] for AA5083-H111 SSM revealed that darker regions inside the stir zone are associated with higher concentrations of piezoelectric particles. Therefore, processing AA2017 generally allowed for a more homogeneous distribution of the piezoelectric particles in the zone influenced by the pin when compared to the AA7075, where it can be noticed darker regions where the particles concentrate. Additionally, the macrographs show evidence that the particles are more evenly distributed in the AS than in the RS.

The macrographs where the region influenced by the shoulder is more pronounced, namely the AA2017-BTO1, AA2017-BTO2, AA7075-BTO1, AA7075-BTO2, and AA7075-PZT1 plates, depicted in Figures 4.7a, 4.7b, 4.8a, 4.8b, and 4.8c, respectively, depict a less homogeneous distribution of particles inside this region, with larger agglomerates, and some even present processing defects. Nevertheless, it is important to reinforce that the specimens subjected to the uniaxial and sensorial behaviour tests have a thickness, t, of 2 mm, measured from the bottom part of the nugget and, therefore, excluding this region.

The macrograph of the AA7075-PZT2 sample revealed two distinct regions inside the zone influenced by the pin. The upper region's micrograph depicts larger agglomerates of particles with less homogeneous distribution (see Figure 4.8d_3), in contrast to the lower region's micrograph, where the agglomerates are smaller and more evenly distributed (see Figure 4.8d_4).

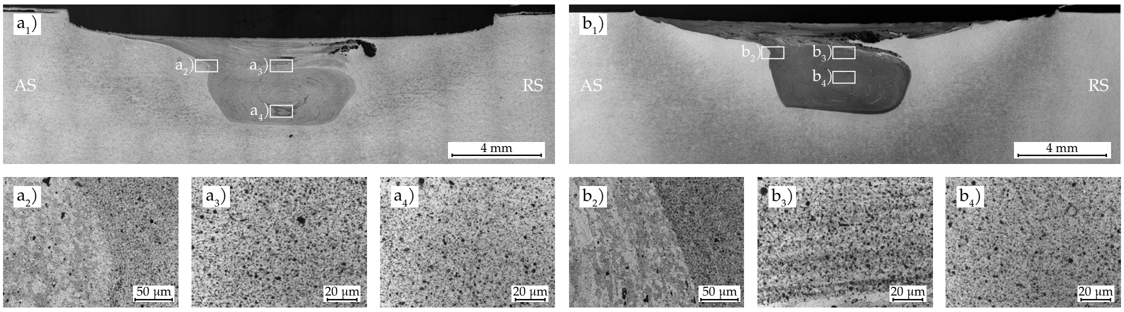

(a) AA2017-BTO1 (b) AA2017-BTO2

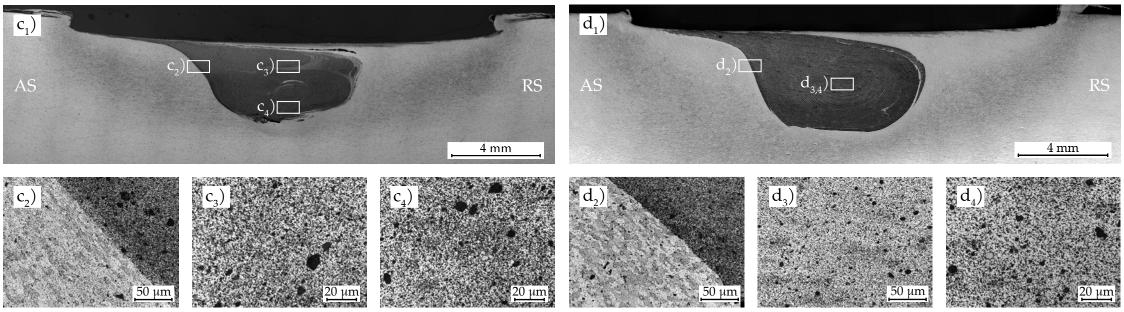

(c) AA2017-PZT1 (d) AA2017-PZT2

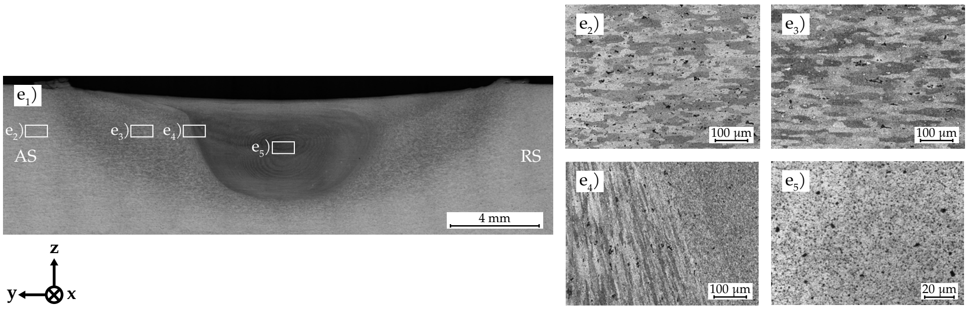

(e) AA2017-R

Figure 4.7: Macro and microstructural characterisation of SSM - AA2017

Figures 4.7e and 4.8e illustrate the key microstructural regions of aluminium processing without the particles. The HAZ presents larger grains when compared to the base material due to the heat generated during the process. The TMAZ depicts the effect of both heat and high strain as the grains are more elongated and deformed. The stir zone shows evidence of dynamic recrystallization since the material experiences high plastic deformation at high temperatures, resulting in grain refinement.

By comparing the grain size within the stir zone before and after the addition of piezoelectric particles, it can be inferred that the incorporation of particles resulted in more pronounced grain refinement in the AA7075 alloy, even though the AA2017 alloy also experiences this. It has already been studied that the use of reinforcement particles plays a crucial role in the fragmentation of grain within the processed microstructure due to localised and non-uniform deformation [60]. Furthermore, using reinforcement

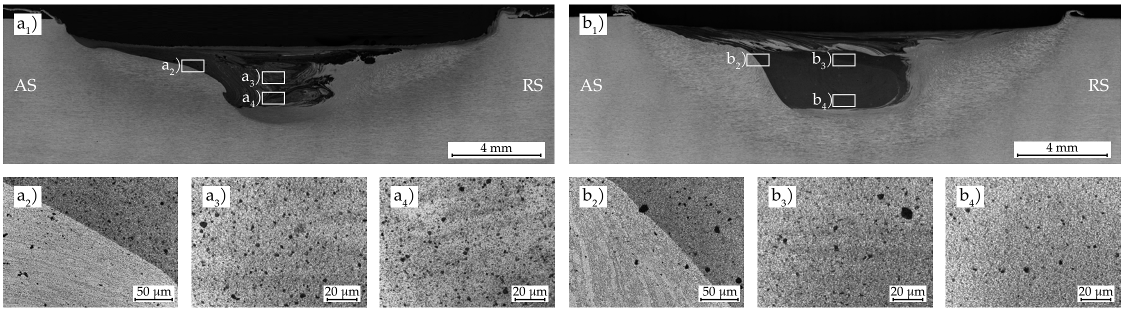

(a) AA7075-BTO1 (b) AA7075-BTO2

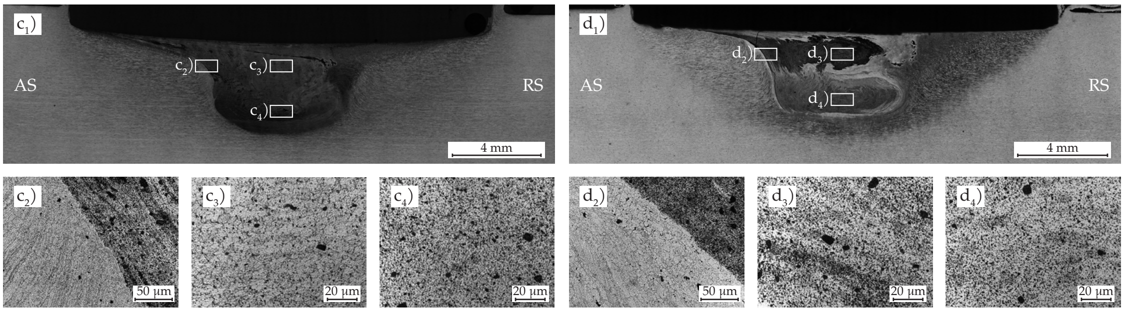

(c) AA7075-PZT1 (d) AA7075-PZT2

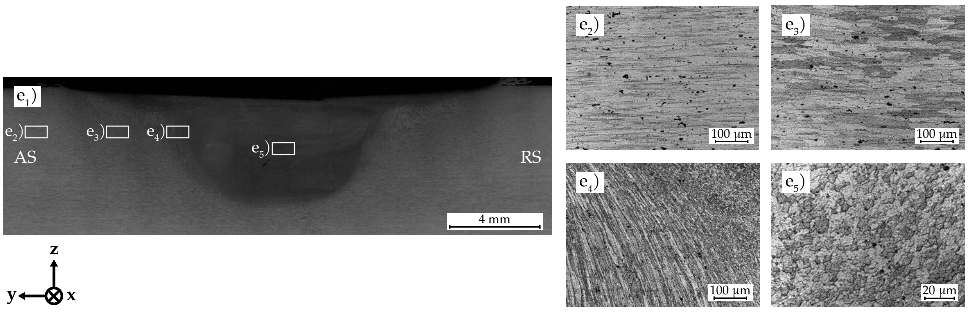

(e) AA7075-R

Figure 4.8: Macro and microstructural characterisation of SSM - AA7075

particles restricts the grain growth of the aluminium matrix grains [61].

The micrographs corresponding to the stir zone of the SSMs processed with PZT revealed the presence of more and larger particle agglomerates compared with the BTO embedment. This can primarily be attributed to the morphology of the PZT particles, which can be an order of magnitude higher in size than BTO particles and depict a tendency to form agglomerates more easily. This difference can impact the grain refinement in the microstructure since smaller particles have a more pronounced effect on grain refinement than larger particles [60].

Figures 4.9a$_{2,3}$ depict the EDX maps at low magnification of the zone influenced by the pin and the shoulder, respectively, in the AA2017-BTO2 sample. A heterogeneous distribution can be observed in the region influenced by the shoulder, with substantial particles' agglomerates, whereas the region influenced by the pin is much more homogeneous and has smaller agglomerates.

EDX maps at higher magnification inside the region influenced by the pin reveal the distribution of particles within this region having punctual small agglomerates, as presented in Figure 4.9b. SEM images revealed the inside structure and morphology of these small agglomerates, and point spectrum analysis confirms the presence of BTO particles confined in the aluminium matrix.

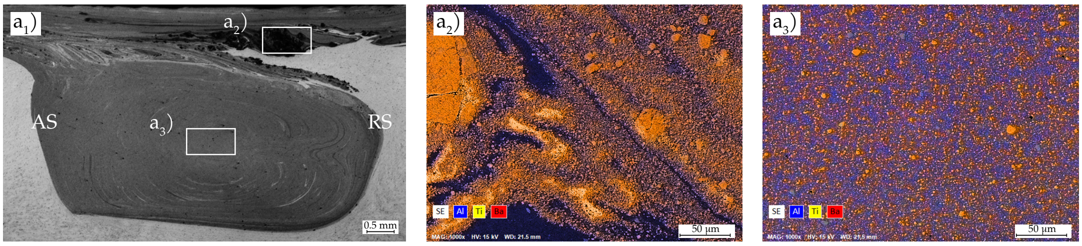

(a) Optical macrograph of stir zone and EDX maps of the zone influenced by the shoulder (a_2) and the zone influenced by the pin (a_3), at x1000 magnification

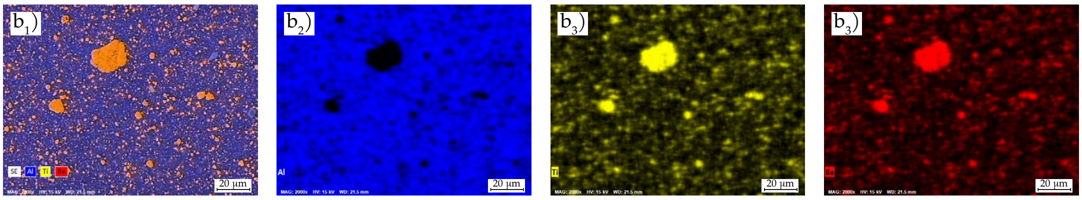

(b) EDX maps of the zone influenced by the pin (a_3), at x2000 magnification

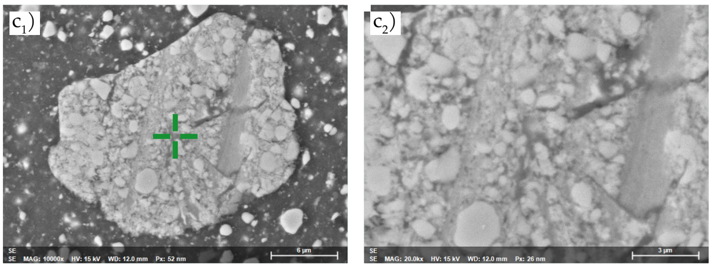

Element	Atomic weight (%)
Aluminium	38.18
Titanium	18.56
Barium	43.26

(c) SEM image and point spectrum analysis of the largest particle agglomerate (b_1) found in the central zone of the nugget

Figure 4.9: SEM and EDX characterisation of particles' distribution of AA2017-BTO2

The EDX map of the AA2017-PZT2 sample at low magnification, presented in Figure 4.10a_2, revealed larger agglomerates than the AA2017-BTO sample. Nevertheless, the particles' overall distribution inside the stir zone's central region remains very homogeneous.

SEM images at higher magnification were taken to characterize the structure and morphology of this agglomerate and its surrounding particles, depicted in Figure 4.10c, and point spectrum analyses were conducted to identify its constituent elements. The chemical composition (wt%) of all the analysed particles corresponds to PZT particles confined inside the aluminium matrix, except particle 5, which appears to be a fragment of the pinned FSP tool, given the high manganese and iron content.

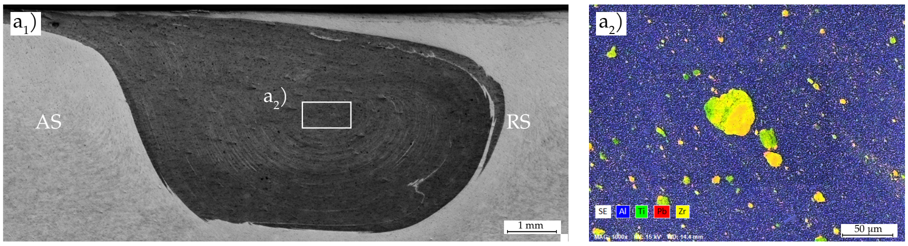

(a) Optical macrograph of stir zone and EDX map of the zone influenced by the pin (a_2), at x1000 magnification

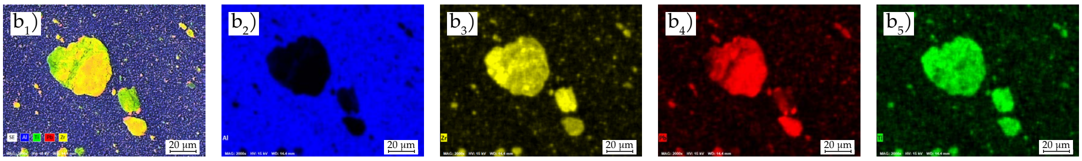

(b) EDX maps of the zone influenced by the pin (a_2), at x2000 magnification

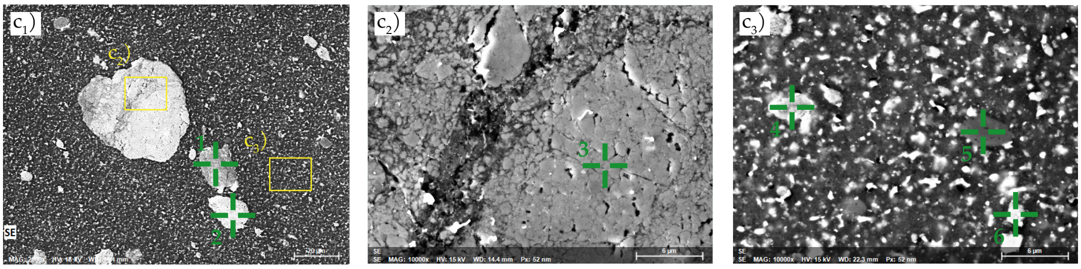

Spectrum	Lead	Zirconium	Titanium	Oxygen	Aluminium	Magnesium	Copper	Manganese	Iron
Particle 1	53.51	23.72	11.11	6.63	4.51	0.52	-	-	-
Particle 2	72.41	11.70	10.44	3.93	1.52	-	-	-	-
Particle 3	80.05	9.03	7.25	2.22	1.44	-	-	-	-
Particle 4	64.14	17.96	8.29	6.08	3.54	-	-	-	-
Particle 5	-	-	-	-	61.96	-	6.48	17.44	14.12
Particle 6	67.99	18.97	7.68	-	5.36	-	-	-	-

(c) SEM images and point spectrum analysis (wt%) of the larger particle agglomerate (b_1) found in the central zone of the nugget and the surrounding particles

Figure 4.10: SEM and EDX characterisation of particles' distribution of AA2017-PZT2

Regarding the embedment of BTO particles in AA7075, SEM and EDX analysis confirmed the presence of some sizeable agglomerates at low magnification, similar in dimensions to the ones found in the AA2017-PZT2 sample, as evidenced in Figures 4.11a and 4.11b. Despite this, the overall distribution of particles is relatively quite homogeneous.

Point spectrum analysis were conducted on a smaller agglomerate, depicted in Figure 4.11c_1. The chemical composition (wt%) shows evidence that particles 2 and 3, present inside the agglomerate, might be a precipitate given their high content of aluminium and iron and a BTO particle, respectively. In contrast, the surrounding particle 1 could be a precipitate, given its high content of silicon and magnesium.

As previously mentioned, the AA7075-PZT2 sample contains two distinct regions inside the stir zone. SEM images, depicted in Figures 4.12$a_{2,3}$, are in accordance with

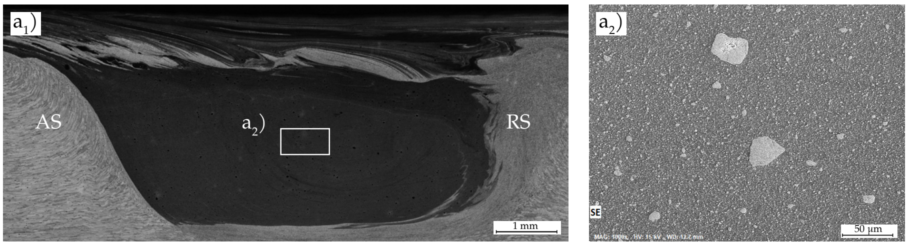

(a) Optical macrograph of stir zone and SEM image of the zone influenced by the pin (a_2), at x1000 magnification

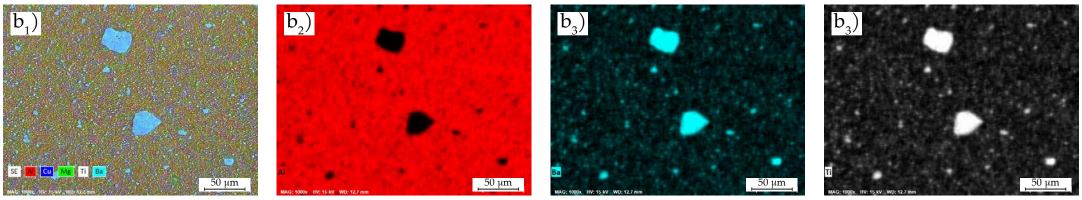

(b) EDX maps of the zone influenced by the pin (a_2), at x1000 magnification

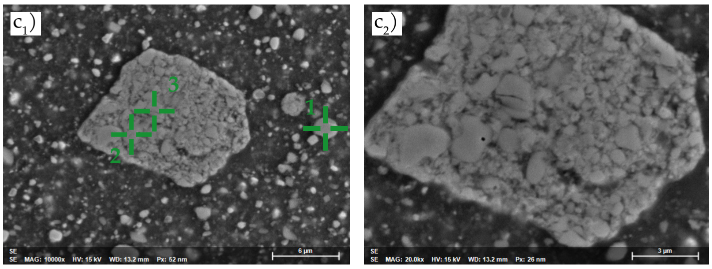

Spectrum	Barium	Titanium	Oxygen	Aluminium	Magnesium	Copper	Silicon	Manganese	Iron
Particle 1	-	-	7.00	-	49.31	-	43.69	-	-
Particle 2	-	-	-	68.81	1.72	6.47	-	0.67	22.33
Particle 3	59.49	24.80	8.00	7.71	-	-	-	-	-

(c) SEM images and point spectrum analysis (wt%) of the fine distributed regions in the central zone of the nugget

Figure 4.11: SEM and EDX characterisation of particles' distribution of AA7075-BTO2

the micrographs presented earlier in this Section, revealing that the upper region has a less homogeneous distribution of particles and with larger agglomerates, while the lower region is quite more homogeneous and has smaller agglomerates. EDX maps of both regions are represented in Figure 4.12b and confirm the differences in particles' distribution.

Point spectrum analyses were conducted in both regions and are presented in Figure 4.11c_2. In the upper region, the particle 4, found inside a large agglomerate, confirms the presence of PZT particles. Regarding the lower region, particle 1 has the chemical composition (wt%) of an expected PZT particle. Particle 2 which is slightly brighter under the SEM, appears to be either a precipitate given the presence of silicon, magnesium and aluminium or an impurity because of the unexpected sodium content, and the dark-appearance particle 3 could be another precipitate with high traces of silicon, magnesium and aluminium.

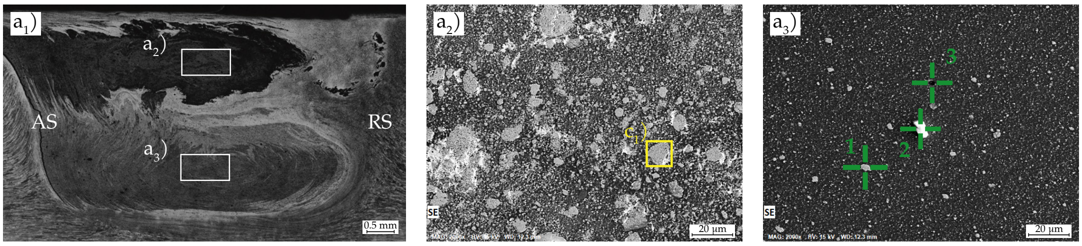

(a) Optical macrograph of stir zone and SEM images of the distinct regions inside the nugget: upper region (a_2); lower zone (a_3), at x1000 magnification

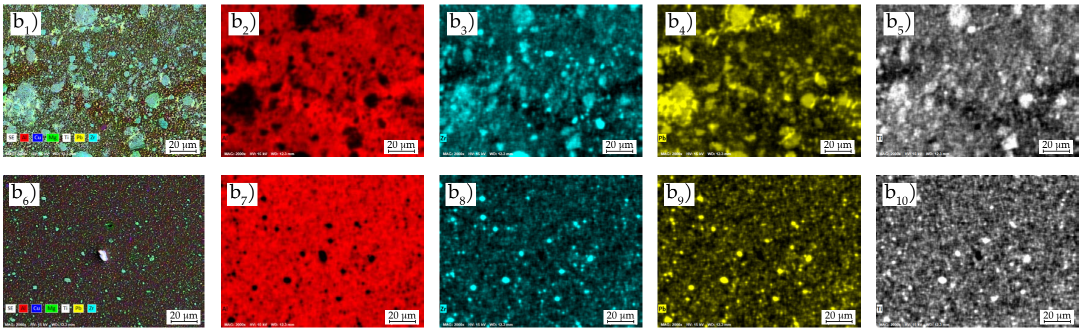

(b) EDX maps of the upper region (b_{1-5}) and the lower region (b_{6-10}) inside the nugget, at x2000 magnification

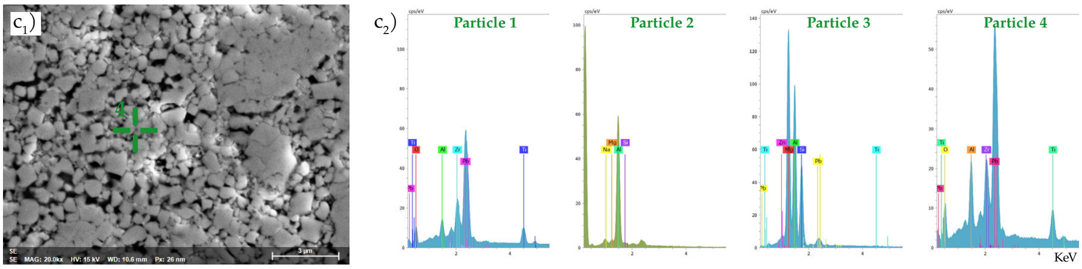

(c) SEM image of particles' agglomerate inside the upper region of the nugget (a_2) and point spectrum graphics of different particles found inside the stir zone

Figure 4.12: SEM and EDX characterisation of particles' distribution of AA7075-PZT2

Figure 4.13 presents the SEM image, the EDX maps and the map spectrum analysis of the AA2017-R sample inside the central region of the stir zone. The small, lighter particles observed in the SEM image appear to be related to precipitates of mainly copper, while the darker particles seem to be related to magnesium-based precipitates.

SEM image and EDX maps of the central region of the nugget of AA7075-R sample with point spectrum analysis are depicted in Figure 4.14. The small, lighter particles appear to be precipitates of Al-Cu-Fe, namely Al_7Cu_2Fe, often seen in 7xxx series aluminium alloys and usually found with bar-like shapes in the base material. During FSP, these precipitates were broken up and then coarsened to spherical particles during the thermal-mechanical cycle [62]. The darker particles also seem to be precipitates since the point spectrum analysis revealed mainly the presence of magnesium, silicon, and aluminium, similarly to what was found in AA7075-PZT2.

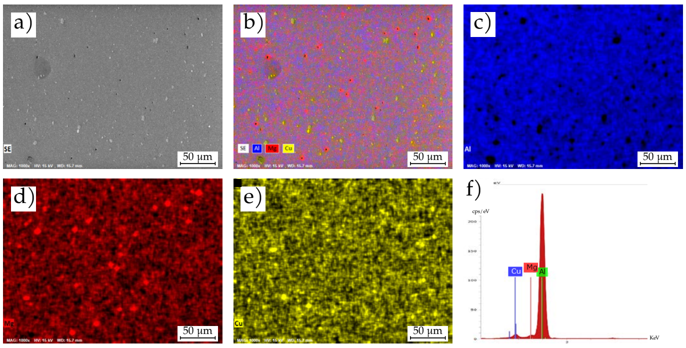

Figure 4.13: SEM image and EDX maps of the centre zone influenced by the pin, at x1000 magnification, and map spectrum analysis

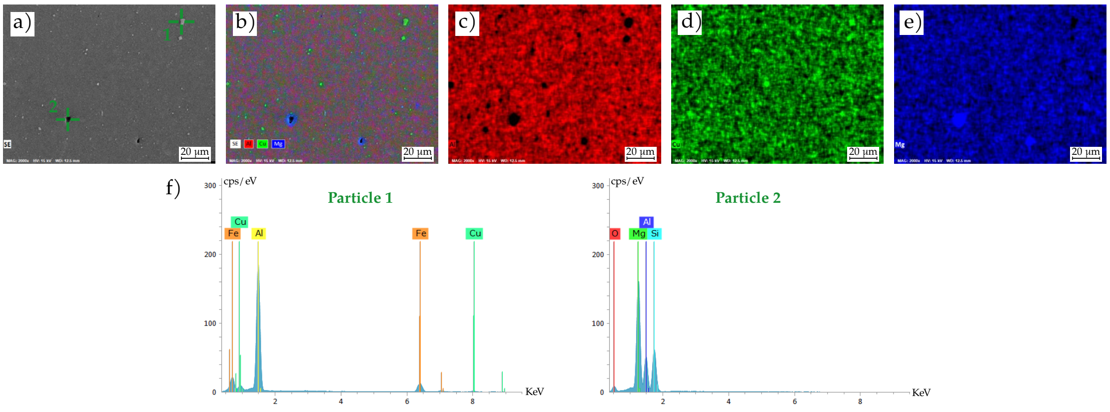

Figure 4.14: SEM image and EDX maps of the centre zone influenced by the pin, at x1000 magnification, and point spectrum analyses of surrounding particles

4.3.2 Microcomputed tomography characterisation

The particles distribution was evaluated through μ-CT analysis and is depicted in Figure 4.15. An inclusion analysis was also conducted to assess the presence of internal agglomerates in the processed zone.

The results for the AA2017, for both BTO and PZT particles, are depicted in Figures 4.15a and 4.15b, respectively, and revealed a relatively good spatial distribution of the particles along the Y and Z directions. However, inside the region influenced by the shoulder, the particles tend to form agglomerates, and the particles' distribution is less homogeneous than in the centre region of the nugget. The AA2017-BTO2 sample revealed agglomerates of particles with higher volume in the region influenced by the shoulder compared to the AA2017-PZT2 sample, where this region is much less extensive and only presents minor agglomerates of particles.

Regarding AA7075, the SSM with BTO particles revealed to have minor agglomerates of particles in the centre region of the nugget along the length, at both Y and Z directions. On the other hand, the embedment of PZT in this alloy introduced many more agglomerates inside the nugget, with higher volumes, especially in the upper region of the nugget in the retreating side.

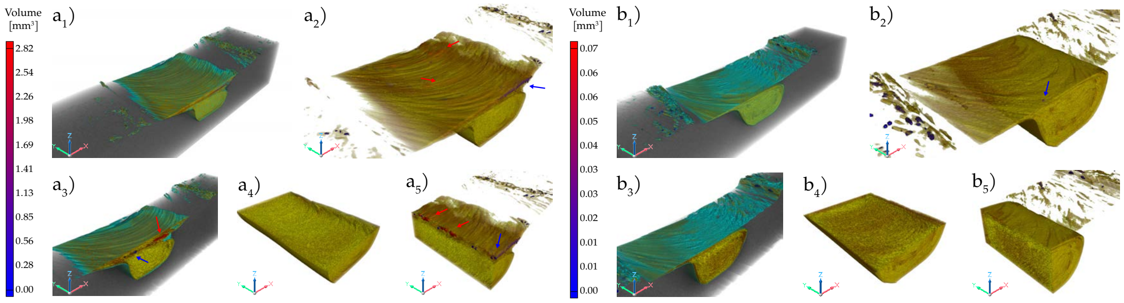

(a) AA2017-BTO2 (b) AA2017-PZT2

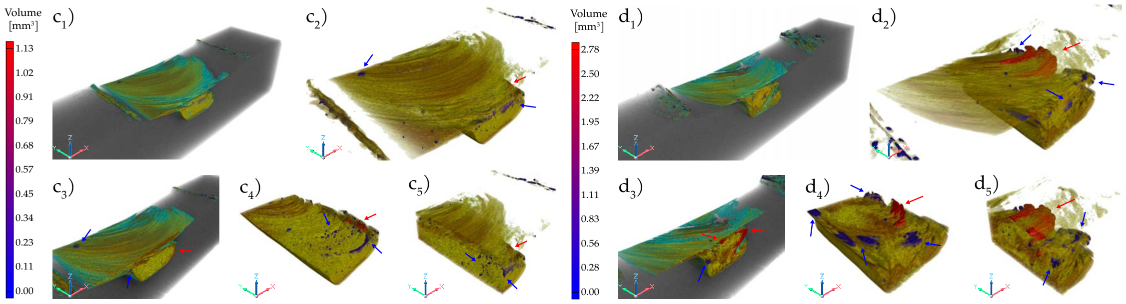

(c) AA7075-BTO2 (d) AA7075-PZT2

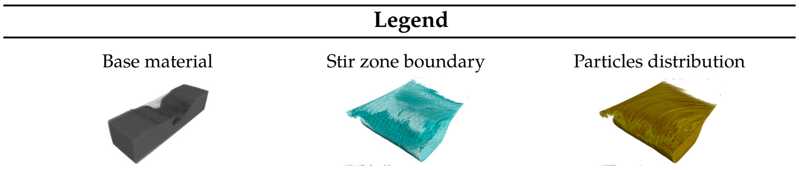

Figure 4.15: μ-CT analysis of SSM: sample (1); particles' distribution (2); transversal cross section of the sample (3); longitudinal cross section of the nugget (4,5)

To assess and fully comprehend the relation between the inclusion analysis and the presence of agglomerates, a comparative analysis, depicted in Figure 4.16, will be conducted between the μ-CT data and the macrographs of the SSMs.

The μ-CT images depict higher concentrations of piezoelectric particles in the retreating side of the nugget and at the separation between the region influenced by the shoulder and the region influenced by the pin for the samples AA2017-BTO/PZT and AA7075-BTO. For these samples and inside these regions, the inclusion analysis revealed localised agglomerates of particles that are distinguishable by the bright white colouration (see Figures 4.16a$_5$-c$_5$). The macrographs of these samples also confirm the presence of agglomerates of particles in these regions, evidenced by a darker colouration.

The AA7075-PZT sample's macrograph (see Figures 4.16d$_{1-2}$) depicts two different regions inside the nugget, one upper region with darker colouration where it can be distinguished localised agglomerates of particles and a lower region less darker without visual indication of agglomerates. The μ-CT images revealed that, indeed, agglomerates of particles can be found inside the upper region and can be distinguishable again by a brighter white colouration.

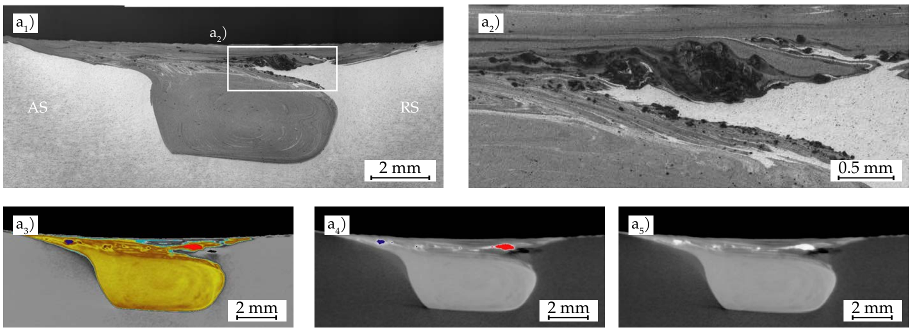

(a) AA2017-BTO2

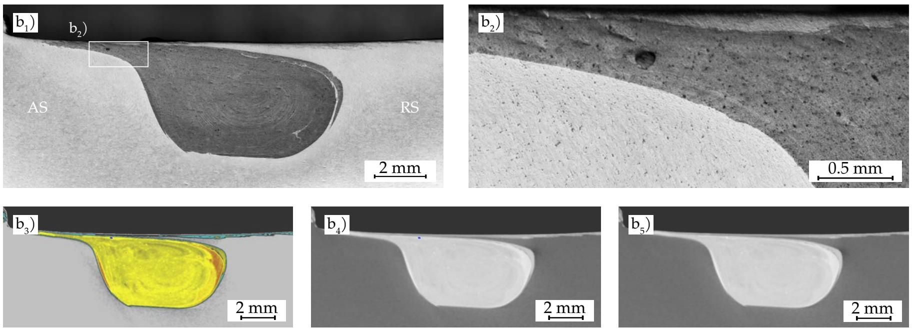

(b) AA2017-PZT2

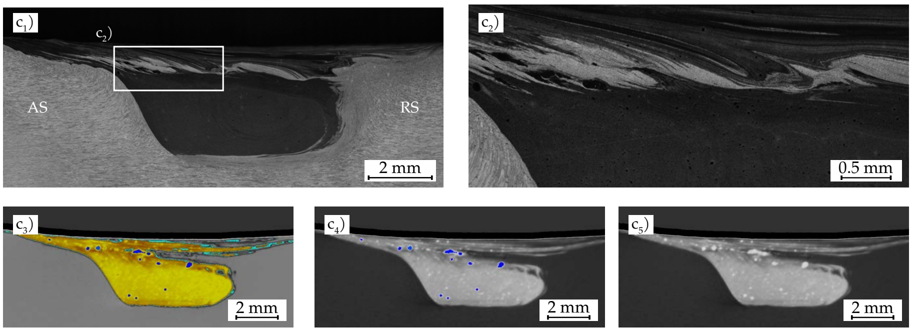

(c) AA7075-BTO2

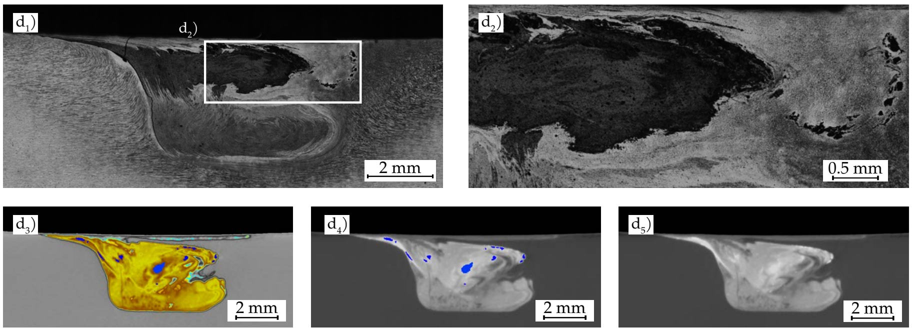

(d) AA7075-PZT2

Figure 4.16: Comprehensive understanding of the inclusion analyses and its relation with the particles' distribution: comparison between the macrographs (indices 1, 2) and μ-CT images (indices 3, 4, 5) of SSMs. The color scale used in the inclusion analysis corresponds to the one adopted in Figure 4.15

4.3.3 Uniaxial tensile tests

The mechanical behaviour of the SSMs was assessed using uniaxial tensile tests. Figures 4.17-4.22 a-b represent the engineering stress/strain curves, while c-e illustrate the fractured samples and the respective fracture surfaces under SEM at different magnifications.

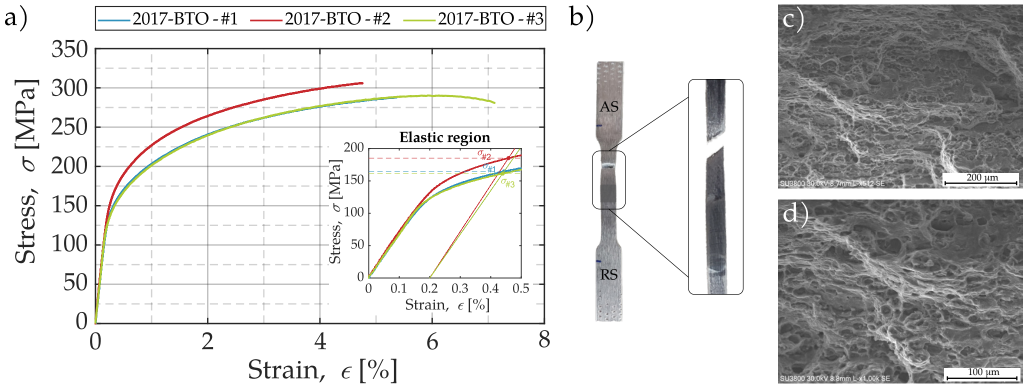

Figure 4.17: Uniaxial tensile tests of AA2017-BTO: engineering stress-strain curves (a); fractured AA2017-BTO-#3 sample (b); fractured surface of SSM (c, d)

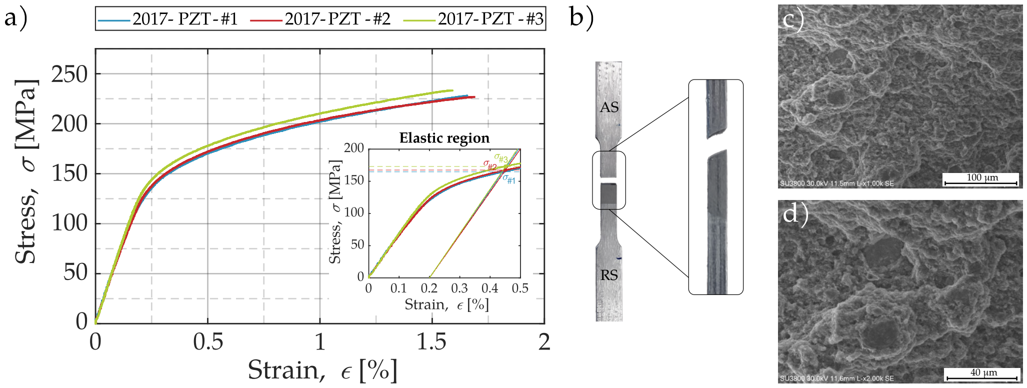

Figure 4.18: Uniaxial tensile tests of AA2017-PZT: engineering stress-strain curves (a); fractured AA2017-PZT-#3 sample (b); fractured surface of SSM (c, d)

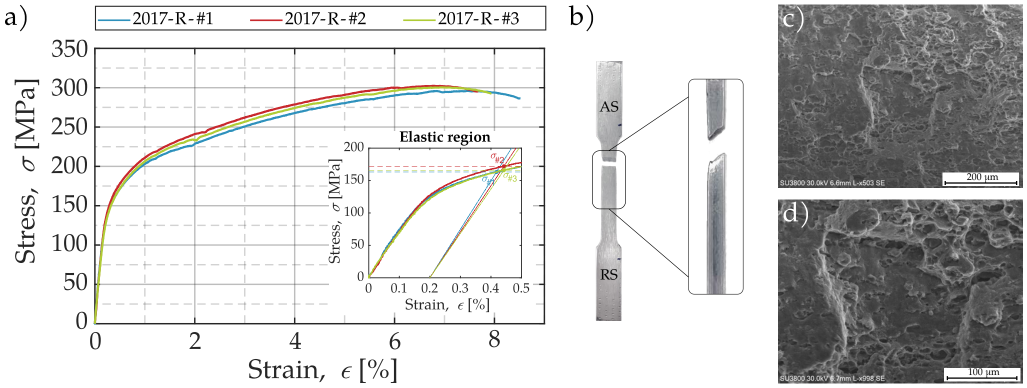

Figure 4.19: Uniaxial tensile tests of AA2017-R: engineering stress-strain curves (a); fractured AA2017-R-#3 sample (b); fractured surface (c, d)

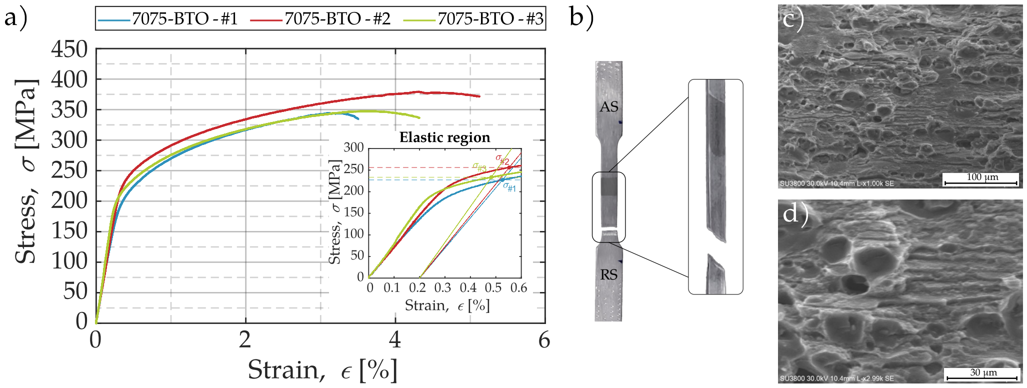

Figure 4.20: Uniaxial tensile tests of AA7075-BTO: engineering stress-strain curves (a); fractured AA7075-BTO-#1 sample (b); fractured surface of SSM (c, d)

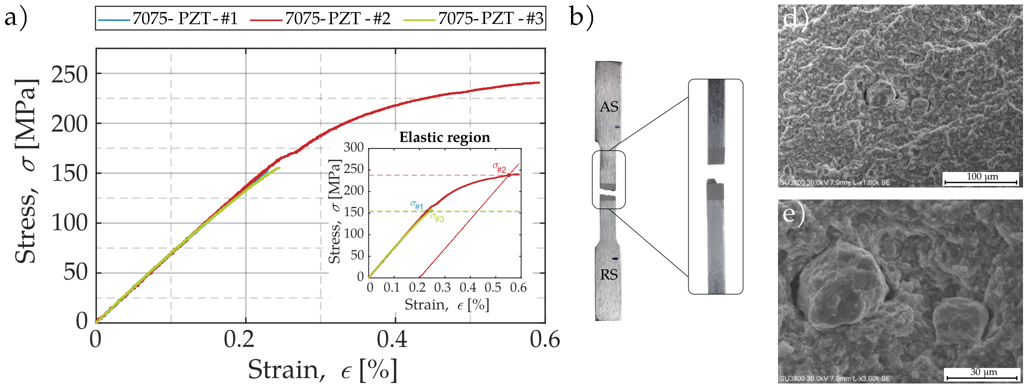

Figure 4.21: Uniaxial tensile tests of AA7075-PZT: engineering stress-strain curves (a); fractured AA7075-PZT-#1 sample (b); fractured surface of SSM (c, d)

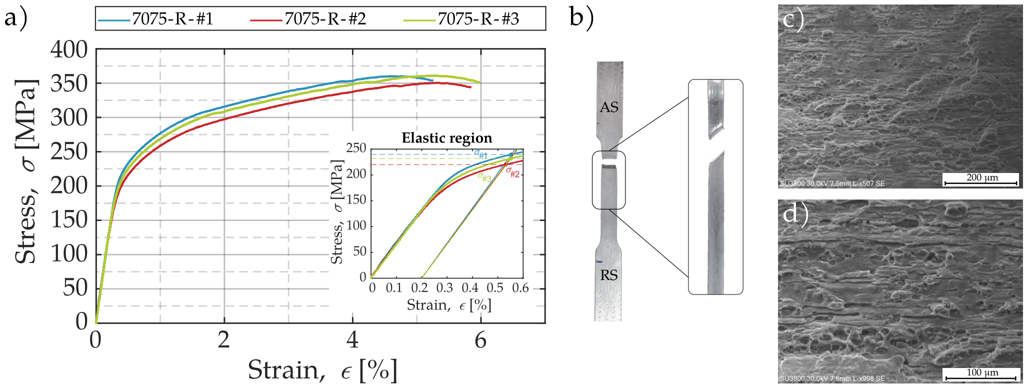

Figure 4.22: Uniaxial tensile tests of AA7075-R: engineering stress-strain curves (a); fractured AA7075-R-#1 sample (b); fractured surface (c, d)

The most significant mechanical properties withdrawn from these tests are summarized in Table 4.4.

Table 4.4: Mechanical properties withdrawn from uniaxial tests

Sample reference	**Yield strength, $\sigma_{0.2}$ [MPa]**	**Modulus of elasticity, E [GPa]**	**Ultimate tensile strength, σ_{UTS} [MPa]**	**Strain at fracture, ε_{f}**
AA2017-BTO-#1	164.64	67.55	287.77	5.37
AA2017-BTO-#2	185.23	71.78	305.85	4.76
AA2017-BTO-#3	161.36	67.55	290.28	7.12
AA2017-PZT-#1	164.72	68.03	227.89	1.66
AA2017-PZT-#2	167.49	66.80	226.74	1.69
AA2017-PZT-#3	173.03	69.01	233.22	1.59
AA2017-R-#1	163.25	74.84	295.96	8.52
AA2017-R-#2	172.04	70.99	302.50	7.67
AA2017-R-#3	165.89	68.48	300.49	7.93
AA7075-BTO-#1	227.36	69.73	344.56	3.51
AA7075-BTO-#2	256.10	72.66	379.03	5.13
AA7075-BTO-#3	233.60	82.78	347.53	4.32
AA7075-PZT-#1	153.15	67.40	153.15	0.23
AA7075-PZT-#2	238.06	67.72	240.74	0.59
AA7075-PZT-#3	155.30	66.47	155.30	0.24
AA7075-R-#1	239.71	67.91	360.23	5.26
AA7075-R-#2	220.09	66.48	350.47	5.85
AA7075-R-#3	231.75	65.88	360.76	5.98

By comparing the processing of plates without and with the incorporation of particles, it is possible to infer that the yield strength, $\sigma_{0.2}$, did not change significantly when particles are introduced into the material. However, the FSP of the plates removes their thermal treatment since the ultimate strength, σ_{UTS}, obtained after processing is much lower than the tensile strength prior to it (refer to Table 3.3).

Incorporating PZT particles causes the SSM to be more brittle than the incorporation of BTO particles, as its extent of fracture is considerably inferior. Figures 4.18 and 4.21 illustrate the fractured specimens containing PZT particles. In contrast to what is observed in Figures 4.17 and 4.20, which regards the incorporation of BTO particles, the fracture in the PZT specimens precisely occurs within the zone containing the particles, i.e. in the stir zone. This phenomenon may indicate a weak bonding between the PZT particles and the aluminium matrix, which could be linked to the particles' more irregular and larger-sized morphology, as discussed in Section 3.2.

The fracture surfaces of the SSM processed with AA2017 can be observed in Figures 4.17-4.19d-e, while those of the processed with AA7075 are highlighted in Figures 4.20-4.22d-e.

In the AA2017 alloy, the failure mode is by ductile fracture, as well-defined dimples can be observed on all fracture surfaces. Additionally, the fracture occurs along a 45° plane. As shown in Figure 4.17, the AA2017-BTO fractured outside the processed zone, similar to the processing without particles depicted in Figure 4.19, leading to the natural similarity between both fracture surfaces. Although the AA2017-PZT fractured at the interface between the processed zone and the base material, it is noted that the failure mode remains unchanged with well-defined dimples and evidence that the fracture occurred through the PZT particles, as they appear to be fractured.

Regarding the processing of the AA7075 alloy, the specimen processed with BTO particles fractured outside the processed zone, similar to the processed plate without particles, and similarly to what occurred in the AA2017 alloy. Thus, the fracture surfaces presented in Figures 4.20 and 4.22 are quite similar. In contrast to the observations in the AA2017 alloy, the fracture surfaces of these specimens exhibit not only well-developed dimples but also a few, although minimal, river marks. Consequently, the failure mode was primarily ductile and similar to the AA2017 alloy, with the fracture surface occurring along planes at 45°. Concerning the processing with PZT particles, where the fracture occurred within the processed zone, it is observed that the matrix of the SSM contains well-developed dimples. However, the irregular and essentially flat nature of the specimen's fractured surface indicates a brittle failure mode. Additionally, Figure 4.21 suggests that the PZT particles are not fractured, which could indicate inadequate bonding between the particles and the SSM matrix.

4.3.4 Microhardness and electrical conductivity characterisation

In order to characterise both the processed and non-processed regions and assess the distribution of particles, microhardness measurements, eddy current testing, and potential drop measurements were conducted on the transverse section (Y direction) of the plates.

Figures 4.23 and 4.24 present the obtained results for AA2017 and AA7075 alloys, respectively.

The hardness measurements can indicate changes in mechanical strength since it is directly proportional to it. Potential drop measurements allow the resistivity and conductivity in processed and non-processed zones to be obtained. Previous works have proved that electrical conductivity is inversely proportional to hardness and, thus, to mechanical strength. Eddy current testing is a technique employed to assess microstructural changes in materials and its complementary to hardness measurements. Therefore, the processed zones have lower electrical conductivity since more grain boundaries reduce the electronic mobility and increase hardness, while the thermal affected zones have higher conductivity and decreased hardness due to the grain growth [3, 60].

Based on the obtained results for the AA2017 alloy, it can be observed that the hardness in unaffected zones, i.e., in base material, remains relatively constant, with average values of 120 HV1.0 and electrical conductivity close to 30 IACS (%). These values are consistent with the expected theoretical values of 118 HV and 34 IACS (%) [63, 64]. As explained previously, maximum electrical conductivity values are recorded in the heat-affected zone

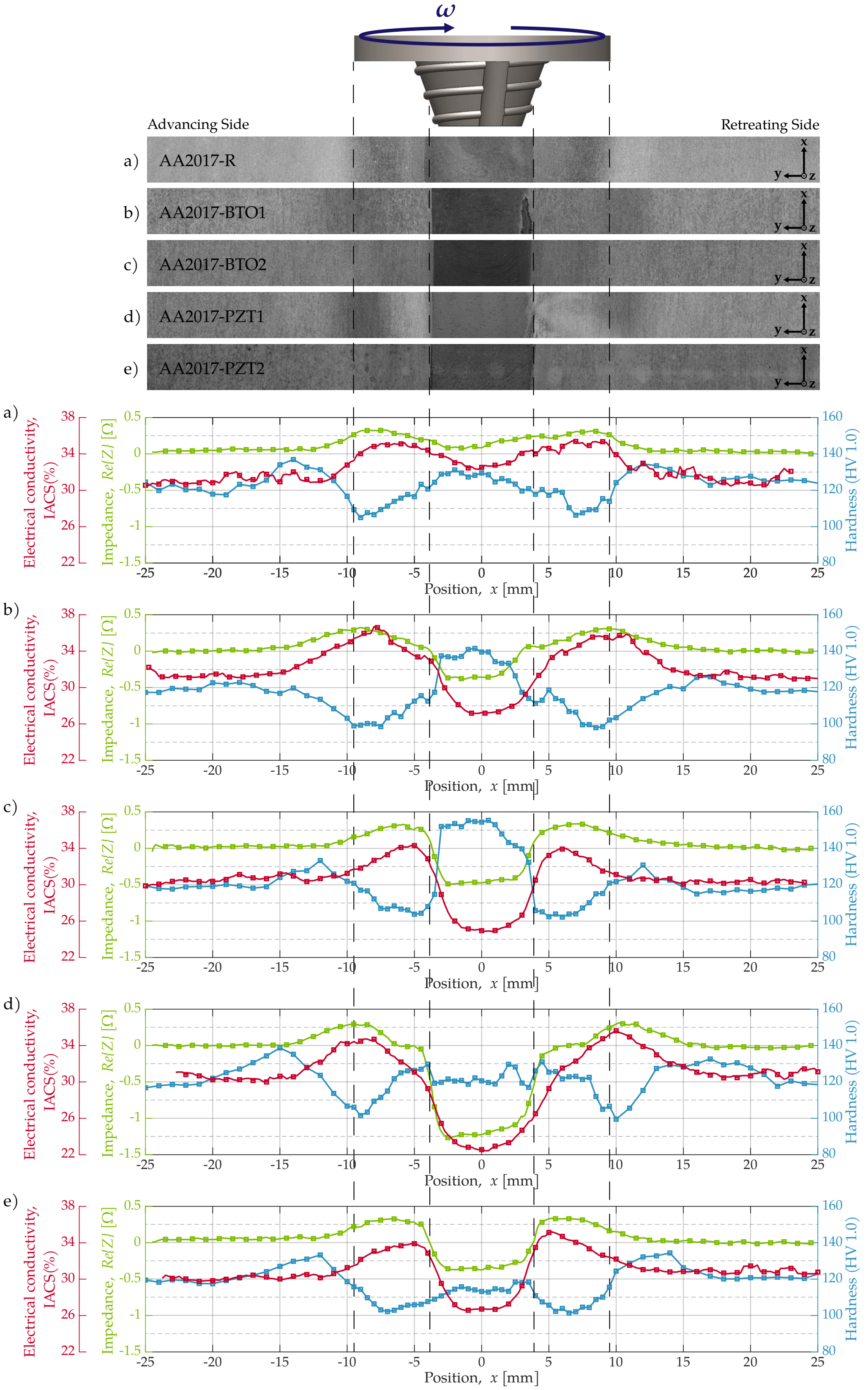

Figure 4.23: Profiles of microhardness, electrical conductivity obtained from potential drop measurements and impedance changes obtained through eddy current testing of AA2017 samples

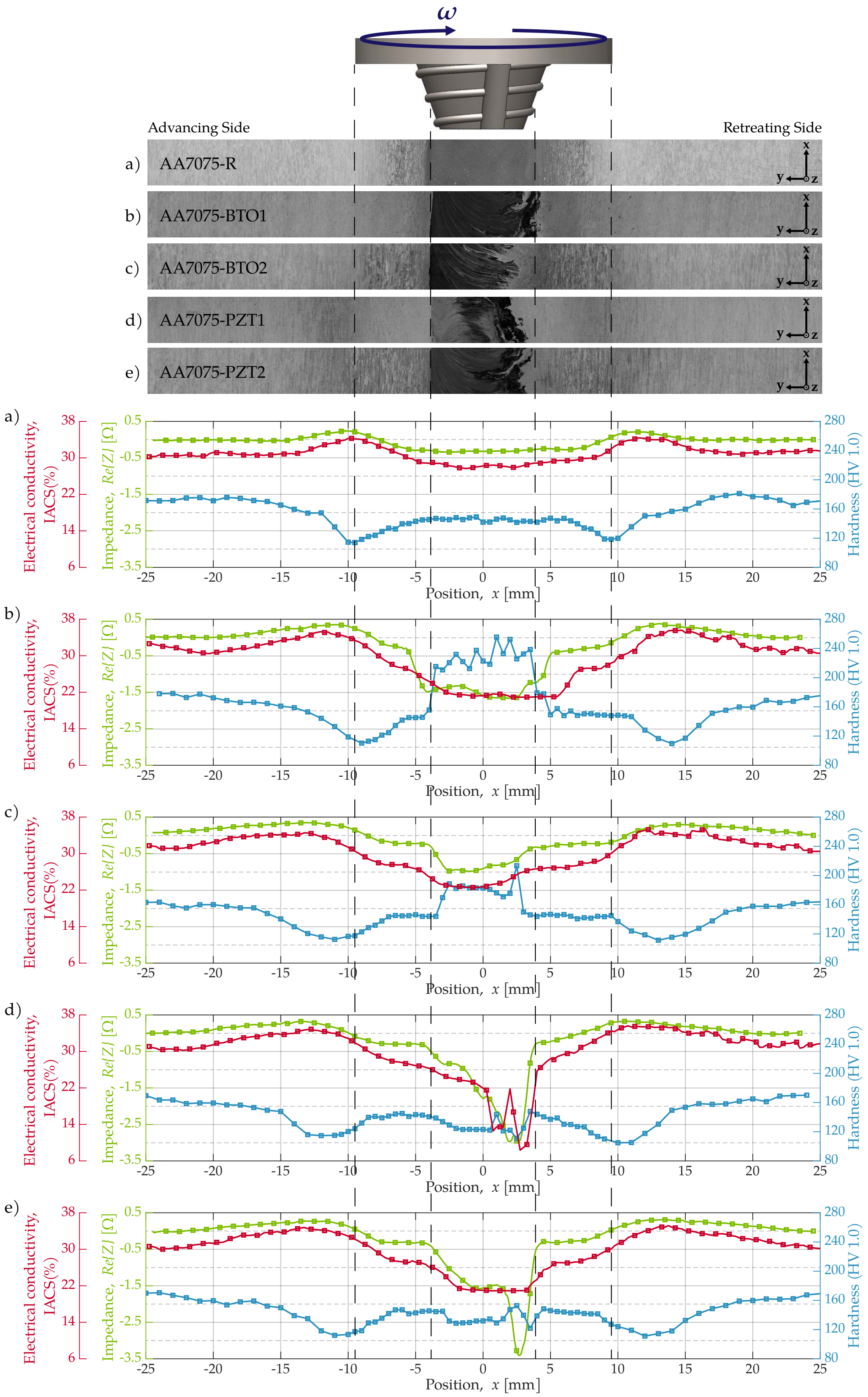

Figure 4.24: Profiles of microhardness, electrical conductivity obtained from potential drop measurements and impedance changes obtained through eddy current testing of AA7075 samples

and, consequently, minimum hardness values due to grain coalescence. Therefore, the low-temperature annealing experienced during processing reduces the strengthening effect caused by the T451 heat treatment. However, a clear distinction in hardness within the stir zone is evident between the BTO and PZT particles processing. The samples processed with BTO particles exhibit an increase in hardness of approximately 20-30 HV1.0, whereas the samples processed with PZT particles even show a hardness decrease of up to 10 HV1.0 in the stir zone. These results are consistent with the micrographs presented in Section 4.3.1. It can be observed that the BTO particles present in the micrographs corresponding to the nugget zone have a significantly smaller size compared to the samples processed with PZT particles. Furthermore, as previously mentioned, smaller particles have a more pronounced impact on grain refinement, which may explain why the hardness increases when processing is conducted with BTO particles and tends to decrease with PZT particles.

Regarding the processing in the AA7075 alloy, both hardness and electrical conductivity in the base material are relatively constant with values of 170 HV1.0 and 32 IACS (%), close to the theoretical values expected of 175 HV and 33.0 IACS (%) [63, 64]. Similarly to the observed in the AA2017 alloy, the HAZ has registered the maximum values of electrical conductivity and minimum values of hardness, proving that the low-temperature annealing experienced during FSP negatively affected the T651 heat treatment. As verified in the AA2017 alloy, the stir zones present a relatively uniform *plateau* with a ≈ 60-100 HV1.0 increase when processing with BTO particles and a ≈ 40 HV1.0 decrease with PZT particles.

In general, both electrical conductivity and impedance change measurements are in good agreement with the obtained hardness profiles.

4.3.5 Sensorial properties assessment

The sensorial properties were assessed by submitting the SSM samples to a set of dynamic loads while measuring their electrical response. Figure 4.25 depicts the process involved in calculating the sensitivity of the SSM samples.

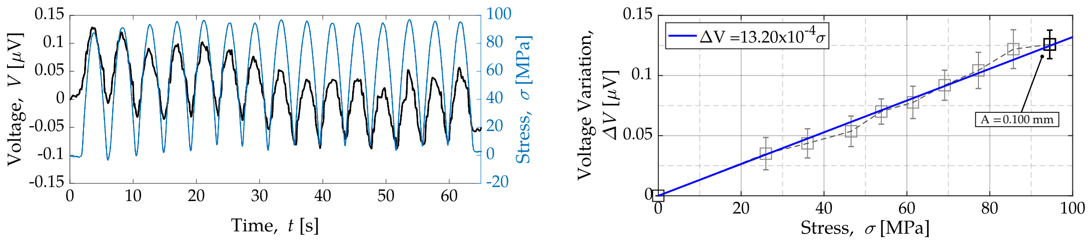

(a) (b)

Figure 4.25: Process involved in calculating the sensitivity of AA2017-PZT: dynamic solicitations at f = 0.125 Hz and A = 0.100 mm, set of 15 cycles (a); sensitivity at f = 0.125 Hz, with all set of amplitudes (b)

These solicitations were replicated for all SSM produced and under different frequencies. Figure 4.26 illustrates the response of AA2017 and AA7075 with the different embedded piezoelectric particles, BTO and PZT.

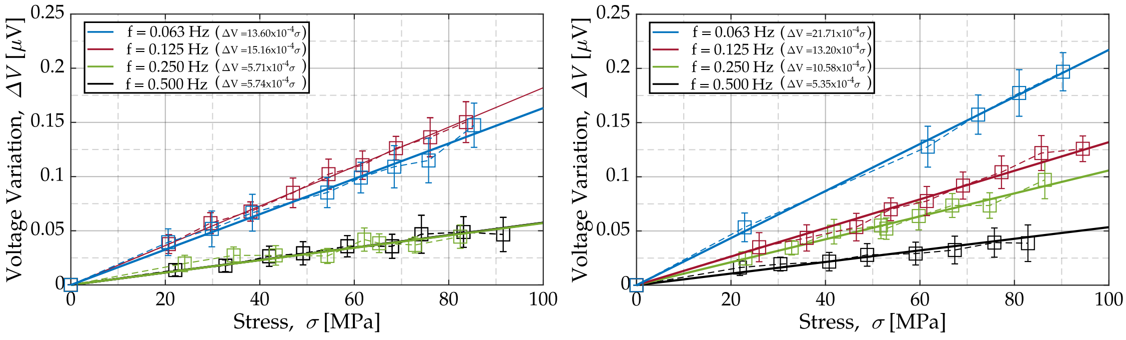

(a) AA2017-BTO (b) AA2017-PZT

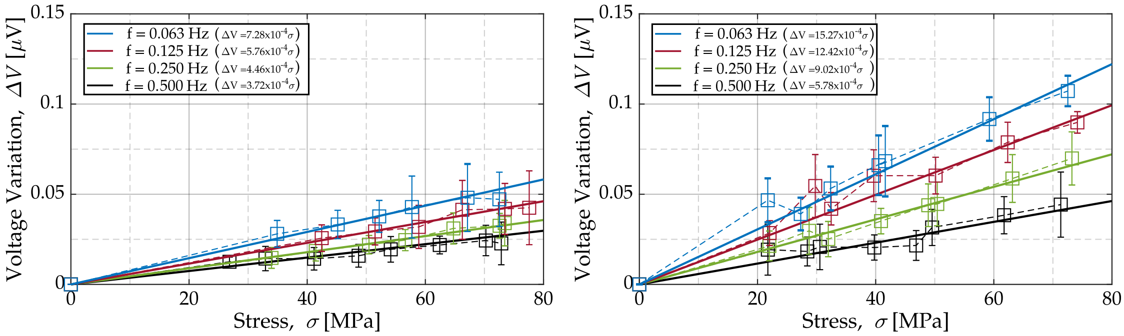

(c) AA7075-BTO (d) AA7075-PZT

Figure 4.26: Electrical response to dynamic loads and effect of different load frequencies on the electric response of the SSM

The results exhibit the expected linear relationship between the applied stress and its electrical response, as previously demonstrated by Ferreira et al. [44]. Higher sensitivities were achieved under the application of lower frequencies except for the AA2017-BTO, where the obtained sensitivity at 0.125 Hz was greater than at 0.063 Hz.

The maximum sensitivity of the AA2017-PZT sample with a value of 21.71×10^{-4}MPa/μV was 43% higher than the maximum sensitivity of AA2017-BTO with 15.16×10^{-4}MPa/μV. Similarly, the AA7075-PZT achieved a maximum sensitivity of 15.27×10^{-4}MPa/μV when compared to AA7075-BTO, which was 52% lower with a value of 7.28×10^{-4}MPa/μV.

An in-depth analysis will be conducted to clarify and establish conclusions regarding the results presented above. Figure 4.27 depicts the effect on sensitivity when embedding different piezoelectric particles into the AA2017 and AA7075 matrix.

These results demonstrate a distinct trend towards achieving higher sensitivities through incorporating of PZT particles compared to BTO particles for the same aluminium matrix, even though the sensitivity obtained in AA2017-BTO at $f = 0.125$ Hz appears to be an outlier point. This might be attributed to the higher piezoelectric constant of PZT particles, $d_{33}/d_{31} = 270/-120$ pC/N, over just $d_{33}/d_{31} = 190/-78$ pC/N of BTO particles. Also, these graphics illustrate the non-linear behaviour between the sensitivity and the applied frequency, with a tendency to enter resonance for lower frequencies than 0.063 Hz.

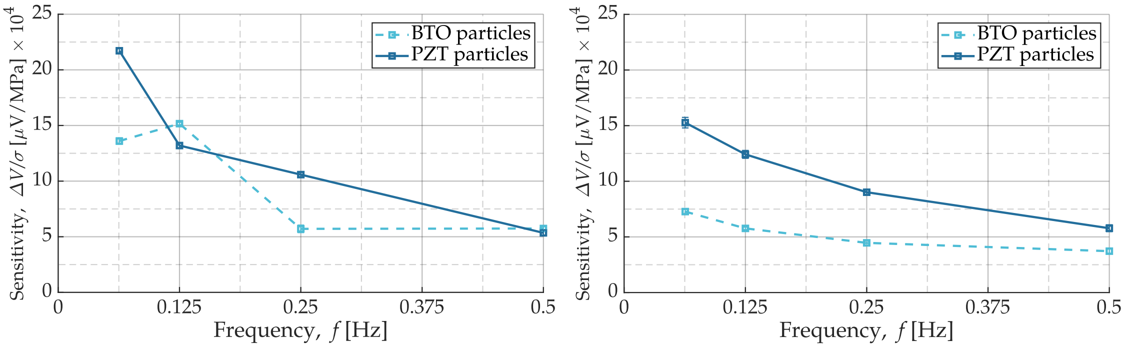

(a) AA2017

(b) AA7075

Figure 4.27: Effect of embedding different piezoelectric particles in the same aluminium matrix on sensitivity

A set of single punctual loads with amplitude, A, of 0.100 mm and at different frequencies, f, were applied to the SSMs to evaluate its response under impact solicitations, as depicted in Figure 4.28.

The SSMs remain responsive under the application of impact loads as expected, exhibiting a response with the same frequency as the solicitation and proving their ability to detect solicitations with different frequencies.

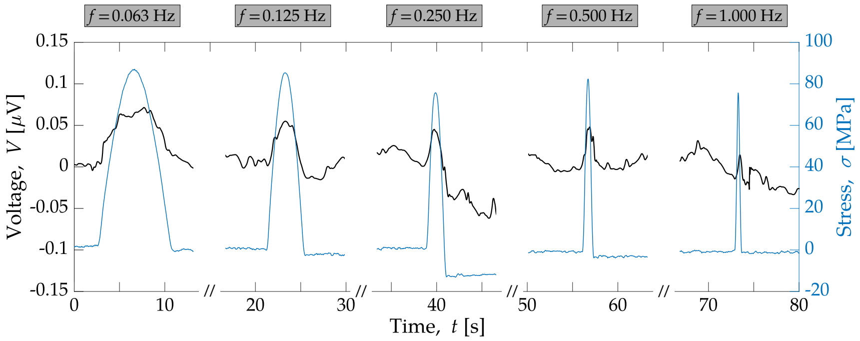

(a) AA2017-BTO

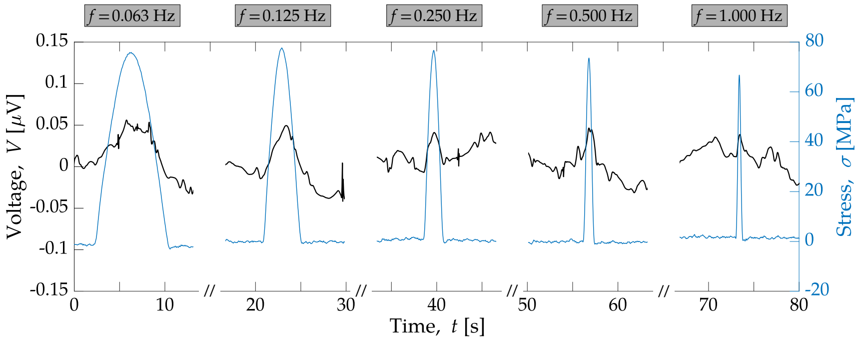

(b) AA2017-PZT

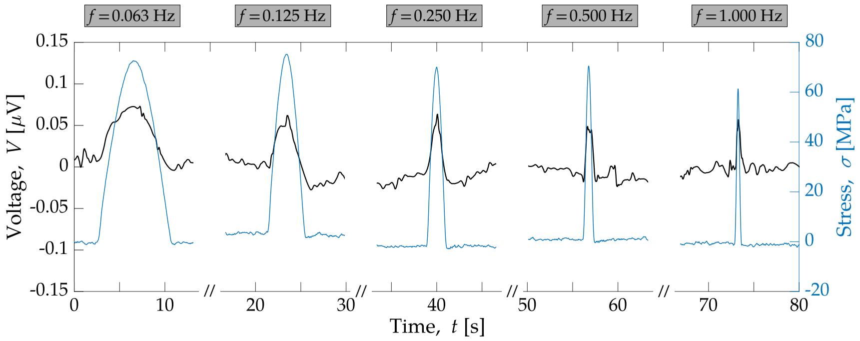

(c) AA7075-BTO

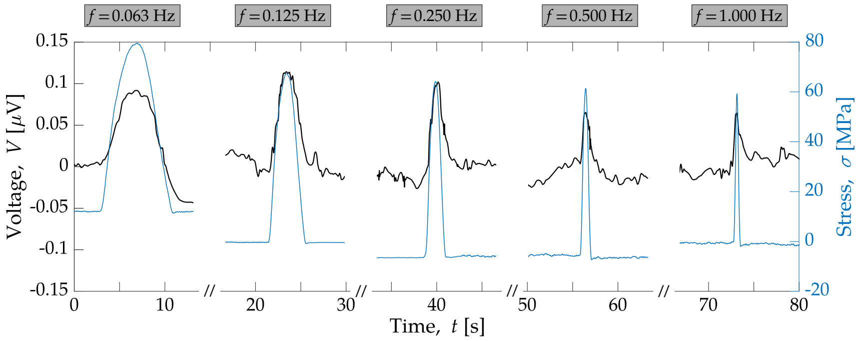

(d) AA7075-BTO

Figure 4.28: Electrical response of SSMs to impact solicitations with different frequencies

5

CONCLUSIONS AND FUTURE WORKS

5.1 Conclusions

This endeavour has successfully proved to be possible to grant sensorial properties to heat-treated AA2017-T451 and AA7075-T651 through the incorporation of BTO and PZT particles, thus resulting in a SSM capable of measuring external solicitations. During the dynamic solicitations, the SSMs exhibit a linear relationship between the applied stress and their electrical response for the same frequency applied. Varying the frequency, the sensitivity of the SSMs exhibits a non-linear behaviour, increasing the sensitivity as the frequency decreases and, therefore, making it more suitable for low-frequency applications.

The temperature measurements demonstrated that adding the piezoelectric particles increases the process complexity, resulting in increased processing temperatures compared to processing without the particles. This is much more evident in the thermal camera measurements since it directly measures the temperature in the stir zone, and it is not influenced by the plate's thermal flow, as experienced by the thermocouples readings. Therefore, the thermal camera measurements revealed that introducing the piezoelectric particles causes an increase of 22-30% in the maximum processing temperatures. Also, the AS thermocouples registered an increase of 7-22% compared to the RS thermocouples for processing passes' maximum temperatures. Since the embedding process is controlled manually, the downward force was regularly adjusted to compensate for minor misalignments of the milling machine. This caused sudden temperature increases and resulted in a significant standard deviation of thermocouples' and thermal camera readings.

The metallographic and physicochemical characterisation allowed a deeper understanding of the particles' distribution. Embedding BTO and PZT particles in AA2017 resulted in a homogeneous distribution of particles in the region influenced by the pin. Concerning the embedment of BTO particles in AA7075, the results were similar, revealing a homogeneous distribution inside the region influenced by the pin. However, the embedment of PZT particles in AA7075 proved challenging, especially in the AA7075-PZT2 sample, where the stir zone presents two distinct regions with different particles' distributions. The reproducibility of the process is more stable in the AA2017 as both plates for each piezoelectric particle provided much more consistent results in terms of particles' distribution than in the AA7075.

The uniaxial tests revealed that embedding the piezoelectric particles increases the material's brittleness, especially regarding the embedment of PZT. The failure mode of the AA2017 SSMs was by ductile fracture, with the fracture surface occurring along planes at 45° and evidence of well-developed dimples under SEM. Regarding the AA7075, the embedment with BTO resulted in a primarily ductile fracture, with the fracture surface occurring along planes at 45°, exhibiting well developed dimples with some evidence of river marks. However, the embedment of PZT resulted in brittle fracture since the fracture surface is perpendicular to the solicitation, even though the fracture surface revealed well-developed dimples in the aluminium matrix surrounding the particles.

Also, the bonding between the PZT particles and the aluminium matrix appears weaker than the embedment with BTO particles, as the fracture in these specimens occurred precisely in the stir zone. The AA2017-PZT specimen fractured at the interface of the nugget and the base material, and the AA7075-PZT specimen fractured in the middle of the nugget.

The $\sigma_{\mathbf{0.2}}$ did not change significantly comparing the embedment with and without the particles. However, the FSP removes the thermal treatment of the plates since the $\sigma_{\mathbf{UTS}}$ is much lower after processing than it was before processing. The negative impact on the heat treatment provoked by the low-temperature annealing experience during FSP is also confirmed due to a decrease in TMAZ's hardness compared to the base material's hardness. The hardness measurements allowed to infer that embedding BTO increased the hardness in the stir zone compared to processing without the particles. Contrastingly, the embedment with PZT resulted in a slight decrease in hardness. This is in accordance with the micrographs and the fracture analysis that revealed larger agglomerates inside the stir zone and fractures occurring within this zone, indicating weaker bonding between these particles and the metal matrix, respectively. In fact, in Section 3.2, SEM was used to characterise the size and morphology of these particles and showed irregularly shaped particles with a clear tendency to form agglomerates. Regarding the eddy current testing and potential drop measurements, both are in accordance with the registered hardness profiles and, therefore, contribute to characterize the particles' distribution and the impact of FSP on microstructure.

The sensorial characterisation of the SSMs revealed an inverse and non-linear relationship between frequency and their sensitivity, proving that these SSMs are most suitable for low-frequency applications. Also, the embedment of PZT particles provided generally better sensitivities than BTO particles and their electrical response's potential varies linearly with the applied stress.

Figure 5.1 presents a comparison between the sensitivities obtained for different aluminium matrices AA2017, AA7075, and AA5083 for each of the embedding piezoelectric particles BTO and PZT. The sensitivities corresponding to the AA5083 were investigated by Ferreira et al. [44].

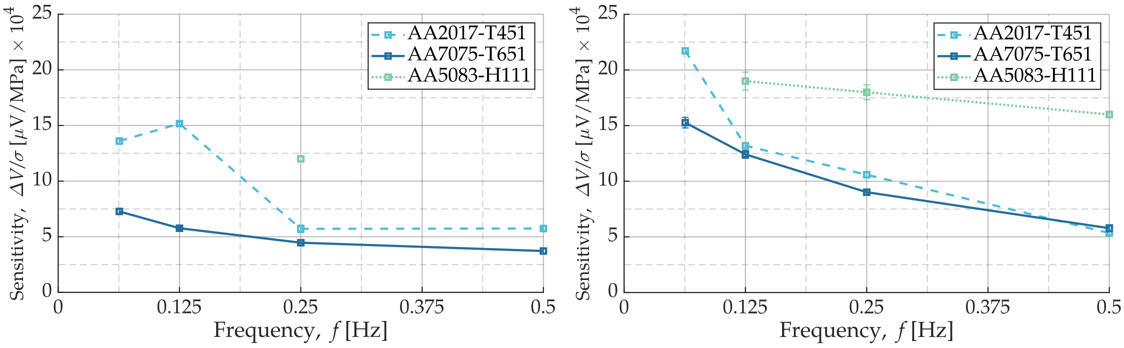

(a) Embedment with BTO particles (b) Embedment with PZT particles

Figure 5.1: Effect of using different aluminium matrices to embed the same piezoelectric particles

A distinct trend is evident toward achieving higher sensitivities using AA5083-H111, followed by the AA2017-T451 and, ultimately, the AA7075-T651. However, the current data obtained through the various characterisation techniques employed in this endeavour cannot clearly justify this observation. The sensitivities of the produced SSMs are a culmination of different factors, each one with its weight, such as the concentration of the piezoelectric particles inside the nugget, the physical properties of the base material such as electrical conductivity, and microstructural differences inside the nugget as a result of using different processing parameters which influences the grain refinement and, consequently, the electrical conductivity inside the stir zone.

5.2 Future works

Using FSP to embed piezoelectric particles in metallic parts represents an innovative breakthrough and is revealed to be very promissory to creating state-of-the-art sensors. Even though this research proved to be able to grant sensorial properties to heat-treated aluminium alloys through the incorporation of these particles, many aspects need further investigation, such as:

- Evaluate the viability of embedding the piezoelectric particles before the heat treatment of the plates. The heat treatment would be performed after embedding, thereby preventing the FSP from removing the heat treatment.
- Increase the reproducibility of the process by automatically controlling the downward force.
- Conduct a deeper evaluation of the impact of precipitates on hardness.
- Evaluate if the particles' concentration varied significantly in the processed plates and the impact it might have had on the sensitivities.

- Evaluate if the electrical conductivity measurements can be used to quantitatively assess the concentration of particles within the stir zone and, therefore, with sensitivity.
- Compare the sensitivity of the specimens when subjected to impact loads and dynamic loads.
- Study the impact of the particles' size on grain refinement and, consequently, on hardness by quantitatively measuring the grain size.
- Investigate the converse piezoelectric effect on the produced SSMs

BIBLIOGRAPHY

[1] J. M. Lourenço. *The NOVAthesis LaTeX Template User's Manual*. NOVA University Lisbon. 2021. URL: https://github.com/joaomlourenco/novathesis/raw/master/template.pdf (cit. on p. ii).

[2] P. M. Ferreira et al. "Embedded Sensors for Structural Health Monitoring: Methodologies and Applications Review". In: *Sensors* 22.21 (2022). DOI: https://doi.org/10.3390/s22218320 (cit. on pp. 1, 2, 10, 16, 17, 19–21).

[3] P. M. Ferreira et al. "Granting Sensorial Properties to Metal Parts through Friction Stir Processing". In: *Measurement* 207 (2023). DOI: https://doi.org/10.1016/j.measurement.2022.112405 (cit. on pp. 1, 2, 4, 15, 18, 21, 23–29, 31, 32, 51).

[4] R. Bouhfid, A. el Kacem Qaiss, and M. Jawaid. *Polymer Nanocomposite-Based Smart Materials: From Synthesis to Application*. 1st ed. Woodhead Publishing, 2020 (cit. on pp. 2, 4–6, 8).

[5] S. J. Rupitsch. *Piezoelectric Sensors and Actuators: Fundamentals and Applications*. 1st ed. Springer, 2019 (cit. on p. 2).

[6] C. M. Hussain and P. D. Sia. *Handbook of Smart Materials, Technologies, and Devices*. 1st ed. Springer, 2022 (cit. on pp. 2, 4).

[7] L. Esther et al. "Smart materials: development of new sensory experiences through stimuli responsive materials". In: 5th STS Italia Conference A Matter of Design: Making Society through Science and Technology, Jun 2014, Milan, Italy. URL: https://hal-emse.ccsd.cnrs.fr/emse-00995958v2/document (cit. on pp. 2, 4, 5).

[8] M. Schwartz. *Encyclopedia of Smart Materials*. 1st ed. Wiley-Interscience, 2002 (cit. on pp. 2, 6, 8–15).

[9] D. M. Addington and D. L. Schodek. *Smart Materials and Technologies: For the Architecture and Design Professions*. 1st ed. Routledge, 2004 (cit. on pp. 2, 4–6, 9, 10).

[10] R. C. Smith. *Smart Material Systems: Model Development*. Society for Industrial and Applied Mathematics, 2005 (cit. on pp. 2, 6–9).

[11] A. K. Ramanathan et al. "Metal structures embedded with piezoelectric PVDF sensors using ultrasonic additive manufacturing". In: *Manufacturing Letters* 31 (2022), pp. 96–100. DOI: https://doi.org/10.1016/j.mfglet.2021.08.001 (cit. on pp. 2, 16, 17).

[12] C. Zhang et al. “Ultrasonic Additive Manufacturing of Metallic Materials”. In: *Metals* 12.11 (2022). DOI: `https://doi.org/10.3390/met12111912` (cit. on pp. 2, 17, 18).

[13] T. Yanaseko, H. Asanuma, and H. Sato. “Characterization of a metal-core piezoelectric ceramics fiber/aluminum composite”. In: *Mechanical Engineering Journal* 2.2 (2015). DOI: `https://doi.org/10.1299/mej.14-00357` (cit. on pp. 2, 21).

[14] T. Yanaseko et al. “Improvement Estimation Accuracy of Impact Detection Using Metal-Core Piezoelectric Fiber/Aluminum Composites”. In: *Advanced Engineering Materials* 21.11 (2019). DOI: `https://doi.org/10.1002/adem.201900550` (cit. on pp. 2, 21).

[15] K. Horikiri et al. “Development of surface oxidized metal fiber/ piezoelectric ceramics/aluminum composite”. In: *Mechanical Engineering Journal* 6 (2019). DOI: `https://doi.org/10.1299/mej.18-00556` (cit. on pp. 2, 21).

[16] Y. Wang et al. “Electromechanical Response and Residual Thermal Stress of Metal-Core Piezoelectric Fiber /Al Matrix Composites”. In: *Sensors* 20 (2020). DOI: `https://doi.org/10.3390/s20205799` (cit. on pp. 2, 21).

[17] M. Lin et al. “SMART Layer and SMART Suitcase for structural health monitoring applications”. In: (2001). DOI: `https://doi.org/10.1117/12.429646` (cit. on pp. 2, 21).

[18] M. S. Hossain et al. “Fabrication of smart parts using powder bed fusion additive manufacturing technology”. In: *Additive Manufacturing* 10 (2016). DOI: `https://doi.org/10.1016/j.addma.2016.01.001` (cit. on pp. 2, 21).

[19] V. F.-G. Tseng, S. S. Bedair, and N. Lazarus. “Acoustic Power Transfer and Communication With a Wireless Sensor Embedded Within Metal”. In: *IEEE Sensors Journal* 18.13 (2018). DOI: `https://doi.org/10.1109/JSEN.2018.2839558` (cit. on pp. 2, 21).

[20] H. Altammar, A. Dhingra, and N. Salowitz. “Ultrasonic Sensing and Actuation in Laminate Structures Using Bondline-Embedded d35 Piezoelectric Sensors”. In: *Sensors* 18.11 (2018). DOI: `https://doi.org/10.3390/s18113885` (cit. on pp. 2, 21).

[21] T. Yanaseko et al. “Vibration Viscosity Sensor for Engine Oil Monitoring Using Metal Matrix Piezoelectric Composite”. In: *Materials* 12.20 (2019). DOI: `https://doi.org/10.3390/ma12203415` (cit. on pp. 2, 21).

[22] A. K. Ramanathan et al. “Metal structures embedded with piezoelectric PVDF sensors using ultrasonic additive manufacturing”. In: *Manufacturing Letters* 31 (2022), pp. 96–100. DOI: `https://doi.org/10.1016/j.mfglet.2021.08.001` (cit. on pp. 2, 21).

[23] A. Concilio et al. *Shape Memory Alloy Engineering: For Aerospace, Structural and Biomedical Applications*. 2nd ed. Butterworth-Heinemann, 2021 (cit. on pp. 2, 6, 7, 15, 16).

[24] S. K. Chilelli, J. J. Schomer, and M. J. Dapino. "Detection of Crack Initiation and Growth Using Fiber Bragg Grating Sensors Embedded into Metal Structures through Ultrasonic Additive Manufacturing". In: *Sensors* 19.22 (2019). DOI: `https://doi.org/10.3390/s19224917` (cit. on pp. 2, 16, 17).

[25] H. C. Hyer, D. C. Sweeney, and C. M. Petrie. "Functional fiber-optic sensors embedded in stainless steel components using ultrasonic additive manufacturing for distributed temperature and strain measurements". In: *Sensors* 52 (2022). DOI: `https://doi.org/10.1016/j.addma.2022.102681` (cit. on pp. 2, 17).

[26] C. Mou et al. "Smart structure sensors based on embedded fibre Bragg grating arrays in aluminium alloy matrix by ultrasonic consolidation". In: *Measurement Science and Technology* 20.3 (2009). DOI: `https://doi.org/10.1088/0957-0233/20/3/034013` (cit. on pp. 2, 19, 20).

[27] A. Hehr et al. "Integrating Fiber Optic Strain Sensors into Metal Using Ultrasonic Additive Manufacturing". In: *JOM* 70 (2018). DOI: `https://doi.org/10.1007/s11837-017-2709-8` (cit. on pp. 2, 19, 20).

[28] A. Hehr et al. "Spatial Strain Sensing Using Embedded Fiber Optics". In: *JOM* 71 (2019). DOI: `https://doi.org/10.1007/s11837-018-3297-y` (cit. on pp. 2, 19, 20).

[29] J. J. Schomer, A. J. Hehr, and M. J. Dapino. "Characterization of embedded fiber optic strain sensors into metallic structures via ultrasonic additive manufacturing". In: *Sensors and Smart Structures Technologies for Civil, Mechanical, and Aerospace Systems 2016*. Vol. 9803. 1. International Society for Optics and Photonics. SPIE, 2016. DOI: `https://doi.org/10.1117/12.2219690` (cit. on pp. 2, 19, 20).

[30] C. M. Petrie et al. "Embedded metallized optical fibers for high temperature applications". In: *Smart Materials and Structures* 28 (2019). DOI: `https://doi.org/10.1088/1361-665X/ab0b4e` (cit. on pp. 2, 19, 20).

[31] H. C. Hyer, D. C. Sweeney, and C. M. Petrie. "Functional fiber-optic sensors embedded in stainless steel components using ultrasonic additive manufacturing for distributed temperature and strain measurements". In: *Additive Manufacturing* 52.2 (2022). DOI: `https://doi.org/10.1016/j.addma.2022.102681` (cit. on pp. 2, 19, 20).

[32] D. Havermann et al. "Temperature and Strain Measurements With Fiber Bragg Gratings Embedded in Stainless Steel 316". In: *Journal of Lightwave Technology* 33.12 (2015). DOI: `https://doi.org/10.1109/JLT.2014.2366835` (cit. on pp. 2, 19, 20).

[33] Y. Li et al. "Ultrasonic embedding of nickel-coated fiber Bragg grating in aluminum and associated sensing characteristics". In: *Optical Fiber Technology* 18.1 (2012). DOI: `https://doi.org/10.1016/j.yofte.2011.09.004` (cit. on pp. 2, 19, 20).

[34] X. Li, A. Golnas, and F. B. Prinz. "Shape deposition manufacturing of smart metallic structures with embedded sensors". In: 3986 (2000-06). DOI: `https://doi.org/10.1117/12.388103` (cit. on pp. 2, 19, 20).

[35] X. C. Li, F. Prinz, and J. Seim. "Thermal behavior of a metal embedded fiber Bragg grating sensor". In: *Smart Materials and Structures* 10 (2001-07). DOI: `https://dx.doi.org/10.1088/0964-1726/10/4/301` (cit. on pp. 2, 19, 20).

[36] X. Li and F. Prinz. "Metal Embedded Fiber Bragg Grating Sensors in Layered Manufacturing ". In: *Journal of Manufacturing Science and Engineering* 125.3 (2003). DOI: `https://doi.org/10.1115/1.1581889` (cit. on pp. 2, 19, 20).

[37] X. Li and F. Prinz. "Analytical and experimental study on noncontact sensing with embedded fiber-optic sensors in rotating metal parts". In: *Journal of Lightwave Technology* 22.7 (2004). DOI: `https://10.1109/JLT.2004.829231` (cit. on pp. 2, 19, 20).

[38] J. J. Schomer and M. J. Dapino. "High Temperature Characterization of Fiber Bragg Grating Sensors Embedded Into Metallic Structures Through Ultrasonic Additive Manufacturing". In: Smart Materials, Adaptive Structures and Intelligent Systems Volume 2: Modeling, Simulation and Control of Adaptive Systems; Integrated System Design and Implementation; Structural Health Monitoring (2017). DOI: `https://doi.org/10.1115/SMASIS2017-3840` (cit. on pp. 2, 19, 20).

[39] T. Grandal et al. "Laser Cladding-Based Metallic Embedding Technique for Fiber Optic Sensors". In: *Journal of Lightwave Technology* 36.4 (2018), pp. 1018–1025. DOI: `https://doi.org/10.1109/JLT.2017.2748962` (cit. on pp. 2, 19, 20).

[40] S. Jinachandran et al. "Fabrication and Characterization of a Magnetized Metal-Encapsulated FBG Sensor for Structural Health Monitoring". In: *IEEE Sensors Journal* 18.21 (2018). DOI: `https://doi.org/10.1109/JSEN.2018.2866803` (cit. on pp. 2, 19, 20).

[41] S. K. Chilelli, J. J. Schomer, and M. J. Dapino. "Detection of Crack Initiation and Growth Using Fiber Bragg Grating Sensors Embedded into Metal Structures through Ultrasonic Additive Manufacturing". In: *Sensors* 19.22 (2019). DOI: `https://doi.org/10.3390/s19224917` (cit. on pp. 2, 19, 20).

[42] A. Hehr et al. "Smart Build-Plate for Metal Additive Manufacturing Processes". In: *Sensors* 20.2 (2020). DOI: `https://doi.org/10.3390/s20020360` (cit. on pp. 2, 19, 20).

[43] H. Alemohammad and E. Toyserkani. "Metal Embedded Optical Fiber Sensors: Laser-Based Layered Manufacturing Procedures". In: *Journal of Manufacturing Science and Engineering* 133.3 (2011). DOI: `https://doi.org/10.1115/1.4004203` (cit. on pp. 2, 19, 20).

[44] P. M. Ferreira et al. "Self-sensing metallic material based on PZT particles produced by friction stir processing envisaging structural health monitoring applications". In: *Materials Characterization* 205 (2023). DOI: `https://doi.org/10.1016/j.matchar.2023.113371` (cit. on pp. 2, 21, 23–25, 35, 38, 55, 59).

[45] Polylanema. URL: `https://www.polylanema.pt/pt/aw-2017-a/` (visited on 2023-02-06) (cit. on pp. 2, 22, 23).

[46] Polylanema. URL: `https://www.polylanema.pt/pt/aw-7075/` (visited on 2023-02-06) (cit. on pp. 2, 22, 23).

[47] J. F. McCabe et al. "Smart materials in dentistry–future prospects". In: *J-Stage: Dental Materials Journal* 28(1): 3743 (2009). DOI: `https://doi.org/10.4012/dmj.28.37` (cit. on p. 4).

[48] A. Hehr et al. "Smart Build-Plate for Metal Additive Manufacturing Processes". In: *Sensors* 20.2 (2020). DOI: `https://doi.org/10.3390/s20020360` (cit. on pp. 17, 18).

[49] K. Li, X. Liu, and Y. Zhao. "Research Status and Prospect of Friction Stir Processing Technology". In: *Coatings* 9.2 (2019). DOI: `https://doi.org/10.3390/coatings9020129` (cit. on pp. 18, 19).

[50] M. K. Gupta. "Friction stir process: a green fabrication technique for surface composites—a review paper". In: *SN Applied Sciences* 2 (2020). DOI: `https://doi.org/10.1007/s42452-020-2330-2` (cit. on p. 18).

[51] AMCO. *Aluminium Temper Overview*. URL: `https://amco-metall.de/fileadmin/downloads/englisch/Temper_aluminium_overview_AMCO.pdf` (cit. on p. 22).

[52] T. F. Scientific. URL: `https://www.thermofisher.com/order/catalog/product/088267.36?SID=srch-srp-088267.22` (visited on 2023-08-31) (cit. on p. 24).

[53] Nanoshel. URL: `https://www.nanoshel.com/sections/nanopowder-compounds` (visited on 2023-08-31) (cit. on p. 24).

[54] M. Lines and A. Glass. *Principles and Applications of Ferroelectrics and Related Materials*. Clarendon Press, 1979 (cit. on p. 24).

[55] P. L. Inácio et al. "Functionalized material production via multi-stack Upward Friction Stir Processing (UFSP)". In: *Materials and Manufacturing Processes* 37.1 (2022), pp. 11–24. DOI: `https://doi.org/10.1080/10426914.2021.1942909` (cit. on p. 25).

[56] C. Vidal et al. “Fabrication of a biodegradable and cytocompatible magnesium /nanohydroxyapatite/fluorapatite composite by upward friction stir processing for biomedical applications”. In: *Journal of the Mechanical Behavior of Biomedical Materials* 129 (2022). DOI: `https://doi.org/10.1016/j.jmbbm.2022.105137` (cit. on pp. 25, 29).

[57] G. L. Sorger et al. “Non-destructive microstructural analysis by electrical conductivity: Comparison with hardness measurements in different materials”. In: *Journal of Materials Science Technology* 35.3 (2019), pp. 360–368. DOI: `https://doi.org/10.1016/j.jmst.2018.09.047` (cit. on p. 30).

[58] T. G. Santos et al. “Microstructural mapping of friction stir welded AA 7075-T6 and AlMgSc alloys using electrical conductivity”. In: *Science and Technology of Welding and Joining* 16.7 (2011), pp. 630–635. DOI: `https://doi.org/10.1179/1362171811Y.0000000052` (cit. on p. 30).

[59] T. Wu et al. “Temperature Monitoring and Material Flow Characteristics of Friction Stir Welded 2A14-t6 Aerospace Aluminum Alloy”. In: *Materials* 12.20 (2019). DOI: `10.3390/ma12203387` (cit. on p. 34).

[60] C. Vidal et al. “Particles’ distribution enhancing in aluminum-based composites produced by upward friction stir processing”. In: *The International Journal of Advanced Manufacturing Technology* 128 (2023). DOI: `https://doi.org/10.1007/s00170-023-11664-y` (cit. on pp. 39, 40, 51).

[61] N. Parumandla and K. Adepu. “Effect of Al2O3 and SiC Nano Reinforcements on Microstructure, Mechanical and Wear Properties of Surface Nanocomposites Fabricated by Friction Stir Processing”. In: *Materials Science - Medžiagotyra* 24.3 (2018). DOI: `https://doi.org/10.5755/j01.ms.24.3.18220` (cit. on p. 40).

[62] J.-Q. Su et al. “Microstructural investigation of friction stir welded 7050-T651 aluminium”. In: *Acta Materialia* 51.3 (2003). DOI: `10.1016/S1359-6454(02)00449-4` (cit. on p. 44).

[63] N. Supply. URL: `https://content.ndtsupply.com/media/Conductivity_Al%20Reference%20Chart.pdf` (visited on 2023-09-17) (cit. on pp. 51, 54).

[64] MatWeb. URL: `https://www.matweb.com/search/datasheet_print.aspx?matguid=53d0e31ee66f4cf9b28abb87c08e4d39` (visited on 2023-09-17) (cit. on pp. 51, 54).